BABAR Analysis Document #40, Version 02

Exclusive Hadronic B Reconstruction to Open Charm Final States

BReco AWG*

July 16, 2000

Abstract

With the data recorded by the *BABAR* detector near $\sqrt{s} = 10.58$ GeV, we have fully reconstructed a variety of hadronic final states containing D^{*-}, D^{*0}, D^0 and D^+ mesons. In this paper, our B candidate reconstruction and selection techniques are described. Finally, a preliminary measurement of the branching ratio in the $B^0 \to D^{*-}\pi^+$ and $B^0 \to D^{*-}\rho^+$ decay modes is reported.

*The *BReco AWG* is formerly known as the Exclusive Hadronic B Decays to Open Charm AWG. People contributing to this document include Ben Brau, Jacques Chauveau, Chih-Hsiang Cheng, Adil Hassan, David Kirkby, Jean-Pierre Lees, **Fernando Martinez-Vidal**, David MacFarlane, Shahram Rahatlou, Patrick Robbe, **Vivek Sharma**, Jan Stark, Gloria Vuagnin, and others.

Contents

1 Introduction

This document reports our efforts to fully reconstruct B meson decays into a variety of channels containing a D^{*+}, D^{*0}, D^{+}, or D^{0} and a π^{-}, ρ^{-}, or a_1^{-}. These are the dominant modes leading to open charm in the final state, all being governed by a tree-level diagram with an external W^{-} emerging as the light hadron state.

The purpose of reconstructing B decays in these modes is two-fold:

- Provide a large sample of $\Upsilon(4S)$ events where one reconstructed B gives a clean tag of the state of the recoil B in the event, with a purity of around 90% or better. Such a sample will be used in studies of B lifetimes, B^0 mixing, and as a means of determining, from the data itself, the effective tagging efficiency through use of information about the decay products of the recoil B. These studies are described elsewhere.

- Provide a new measurement of the absolute branching ratios for the primary B decay channels, as well as the relative branching ratios for a large variety of related modes. Eventually, given the large data sample being accumulated by *BABAR*, we should be able to undertake a thorough study of the resonant substructure for many of these decays, including production of excited charm states.

The channels currently under study are listed in Table 1. [1] The D^{*+} is reconstructed in the mode $D^0\pi^+$, while for the D^{*0} we use both $D^0\pi^0$ and $D^0\gamma$. The D^0 is found in the modes $K^-\pi^+$, $K^-\pi^+\pi^0$, $K^0_S\pi^+\pi^-$, and $K^-\pi^+\pi^+\pi^-$. For the D^+, the channels $K^-\pi^+\pi^+$ and $K^0_S\pi^+$ are included. B candidate reconstruction is based on standard selection techniques and background suppression methods, implemented using Composition Tools. The data used for the current study was obtained using the *BABAR* detector, operating in the PEP-II storage ring at energies near $\sqrt{s} = 10.58$ GeV. They constitute a sample equivalent to 3.8 fb^{-1} recorded over the period February 28 to May 3, 2000.

B Mode
$\overline{B}^0 \to D^{*+}\pi^-$
$\overline{B}^0 \to D^{*+}\rho^-$
$\overline{B}^0 \to D^{*+}a_1^-$
$\overline{B}^0 \to D^{+}\pi^-$
$\overline{B}^0 \to D^{+}\rho^-$
$\overline{B}^0 \to D^{+}a_1^-$
$B^- \to D^{*0}\pi^-$
$B^- \to D^{0}\pi^-$

Table 1: B decay channels examined in this analysis.

This report is organized as follows: Section 2 will describe the data and Monte Carlo samples and the event pre-selection techniques, Section 3 will provide a detailed description

[1] Here, and throughout this document, we use the convention that a particular candidate state also implies the charge conjugate state is included.

of the final candidate selection requirements, Section 4 will summarize the observed signals in B^0 channels, Section 5 will do the same for B^+ modes, Section 6 will describe the additional requirements, systematic error studies, and cross checks employed to extract a result for the absolute branching ratios in the modes $\overline{B}^0 \to D^{*+}\pi^-$ and $\overline{B}^0 \to D^{*+}\rho^-$, and Section 7 will draw conclusions. The present version of this report is a snapshot of the analysis based on a preliminary sample of the full dataset. Many additional studies and Monte Carlo comparisons are planned for the next iteration, which will be based on the full Osaka sample.

2 Data Sample and Pre-Selection Criteria

2.1 Data Samples

This section describes the data samples used for this selection and to study backgrounds, as well as the Monte Carlo event samples used to study and optimize the selection. The data sample is referred to as the "enlarged Elba" sample since it was originally defined for the Elba Collaboration meeting (May 28–31).

2.1.1 Good Run Criteria

"Good runs" are selected using the following information recorded in the electronic logbook and OPR book-keeping database [9]:

- the run type should be "Colliding Beams",
- all subdetectors should be "on",
- the global data quality entered by the Data-Quality shift taker should be "good",
- the recorded luminosity should be non-zero, and
- the OPR processing status should be "done".

Some further checks are made on the self consistency of the electronic logbook information for a run, and by checking some OPR monitoring plots (by hand for now).

2.1.2 Elba Data Sample

The enlarged Elba data sample consists of 592 runs[2] in the range 12118–13091, for a total integrated luminosity of about 3.8 fb^{-1}. This sample is not homogeneous, but can be divided into a few reasonably homogeneous sub-samples. The main effects to consider are the center of mass energy and the quality of the silicon vertex detector's (SVT) internal alignment. Table 2 summarizes the main statistics for each sub-sample. Figure 1 shows the run-by-run offsets of the center of mass energy relative to the average values for each sub-sample given in Table 2.

[2]Runs 13084 and 13086 were in the original sample definition and then later discovered to be bad. They are not included here.

Set	Recorded	Run Range	Int.Lumi.	Avg. $\delta\sqrt{s}$
1	Feb 28–Mar 19	12118–12417	954 pb^{-1}	+5.0 MeV
2	Mar 20–Apr 7	12419–12680	1277 pb^{-1}	+5.0 MeV
3	Apr 8–Apr 11	12683–12722	285 pb^{-1}	-37.1 MeV
4	Apr 12–Apr 20	12747–12873	682 pb^{-1}	+0.0 MeV
5	Apr 20–May 3	12874–13091	883 pb^{-1}	-0.1 MeV
			4081 pb^{-1}	

Table 2: Summary statistics for the sub-samples of the enlarged Elba dataset. Dates are all in the year 2000. Only good runs in the run ranges are included. Average center of mass energies are calculated from the PEP-II beam energies, relative to the nominal $\Upsilon(4S)$ mass of 10.580 GeV/c^2.

2.1.3 Changes to the Reconstruction Code

The runs in the enlarged Elba sample were processed in OPR by five different releases, as shown in Table 3. For the purposes of this selection, the only significant changes were introduced in release P8.6.3a [11]:

- fixes to splitting clusters with closely spaced calorimeter bumps (less than about 15 cm),
- track-bump matching is now done without any energy cutoff (in earlier releases, all low-energy bumps would be neutral), and
- loosen momentum cuts for π^0 lists and tighten the π^0 mass window.

The changes to the π^0 selection do not affect this data sample since the most recent cuts (those in P8.6.3a) were applied in making the ntuples for the full Elba sample.

Release	Runs	On Peak	Off Peak
P8.6.1,a,b	179	954 pb^{-1}	0 pb^{-1}
P8.6.2a	26	204 pb^{-1}	0 pb^{-1}
P8.6.2b	107	832 pb^{-1}	0 pb^{-1}
P8.6.2d	199	1317 pb^{-1}	285 pb^{-1}
P8.6.3a	81	488 pb^{-1}	0 pb^{-1}

Table 3: Releases of OPR used to process the enlarged Elba event sample.

Some of the plots in this note refer to a typical run: we choose run 12917 from sub-sample 5. Table 4 summarizes the main parameters of this run.

2.1.4 Monte Carlo Samples

The Monte Carlo samples used in this report are taken from productions based on the releases 8.6.2d and 8.6.3a. The background events provided for these samples correspond

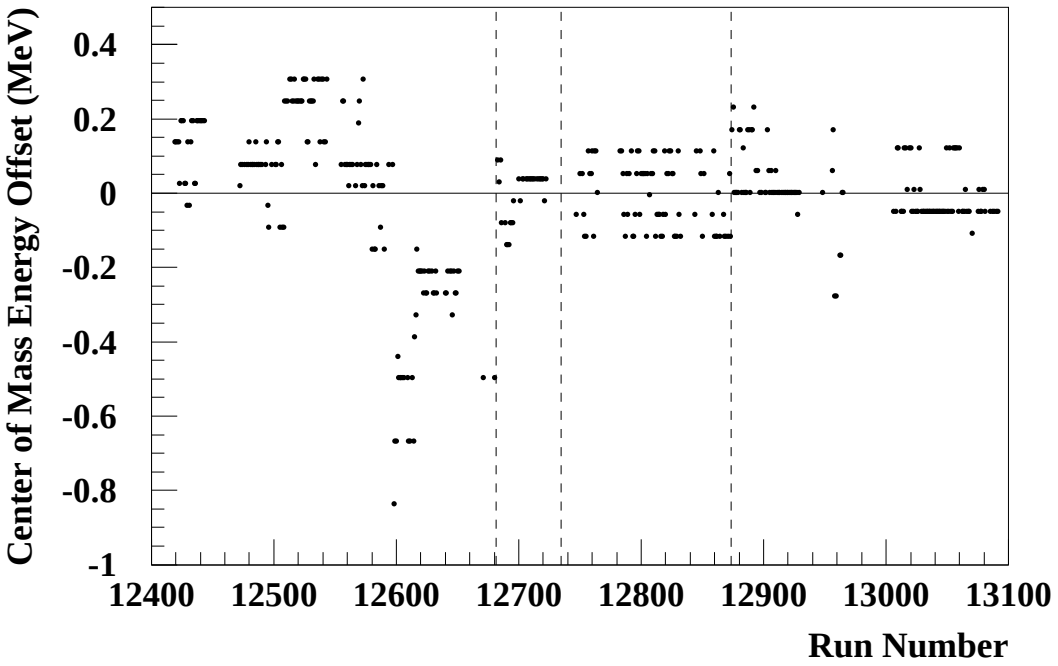

Figure 1: Run by run offsets of the center of mass energy calculated from the PEP-II beam energies relative to the average center of mass energies for each Elba sub-sample given in Table 2. Vertical dashed lines show the boundaries between each Elba sub-sample.

to February and March 2000 conditions respectively. The main deficiencies in the detector simulation are in the area of Drift Chamber single cell efficiencies and tracking performance. The 8.6.2d release used a nominal 95% single cell efficiency. Proper modeling of the dead regions in the chamber was implemented with 8.6.3a. However, the number of active hits on track is not a good match to that observed in the reconstruction of $\Upsilon(4S)$ data, nor is the overall Drift Chamber tracking inefficiency well reproduced. Discrepancies in the predicted efficiencies at the level of 5-10% per track should be anticipated, with a strong dependence on the polar angle observed in data but not Monte Carlo. These discrepancies will be under better control in the upcoming 8.6.4b Monte Carlo production.

HER Energy	8.9711 GeV
LER Energy	3.1193 GeV
CM Energy	10.580 GeV
Integrated Luminosity	12.7 pb^{-1}
isPhysicsEvents	199,648
Dstarlnu Events	10,386
Flagging Rate	$5.20 \pm 0.05\%$

Table 4: Parameters of the typical run 12917, recorded from 8:06–11:06am on April 23, 2000.

2.2 Event Pre-Selection

Pre-selection starts from events assigned to the *isPhysicsEvents* stream in online prompt reconstruction (OPR). This stream includes events assigned to any of the physics sub-streams by the background filter (BGF). We do not make any explict requirement that events belong to the *BGFMultiHadron* sub-stream, but in practice, our requirements on charged track multiplicity and event shape are tighter than those for the *BGFMultiHadron* list (3 or more tracks, $R_2 < 0.98$). One subtlety to consider is that the track definition used by the background filter is not strictly looser than the definitions used in analysis, because it is based only on drift chamber information.

2.2.1 Reconstruction Lists

The particles observed in the detector from the decay modes used in this selection are $K^{\pm}$, $\pi^{\pm}$, $e^{\pm}$, $\mu^{\pm}$, and γ. The basic objects corresponding to these particles and reconstructed in the detector are organized into the following lists, according to whether they are charged or neutral [10]:

- *ChargedTracks*: All tracks reconstructed in the drift chamber and/or the vertex detector, with parameters determined using a $\pi^{\pm}$mass hypothesis.
- *GoodTracksVeryLoose*: A subset of the *ChargedTracks* list containing tracks with:
  1. a maximum momentum measured in the lab frame of 10 GeV/c, and
  2. a distance of closest approach to the per-run nominal beam spot centroid of $\sqrt{\Delta x^2 + \Delta y^2} < 1.5$ cm, and $|\Delta z| < 10$ cm.
- *GoodTracksLoose*: A subset of the *ChargedTracks* list containing tracks with:
  1. a minimum transverse momentum of 100 MeV/c, and
  2. at least 20 hits recorded in the drift chamber, out of a possible maximum of 40 hits for tracks perpendicular to the beam pipe.
- *GoodTracksTight*: A subset of the *GoodTracksLoose* list containing tracks with:
  1. a tighter distance of closest approach requirement of $\sqrt{\Delta x^2 + \Delta y^2} < 1$ cm, and $|\Delta z| < 3$ cm.
- *CalorNeutral*: All "bumps" (local maxima of calorimeter energy deposit) not matched with any track, with parameters determined using a photon mass hypothesis.

Figure 2 compares some inclusive charged-track distributions for the successively tigher track requirements. Figure 3 shows similar distributions for neutral calorimeter bumps.

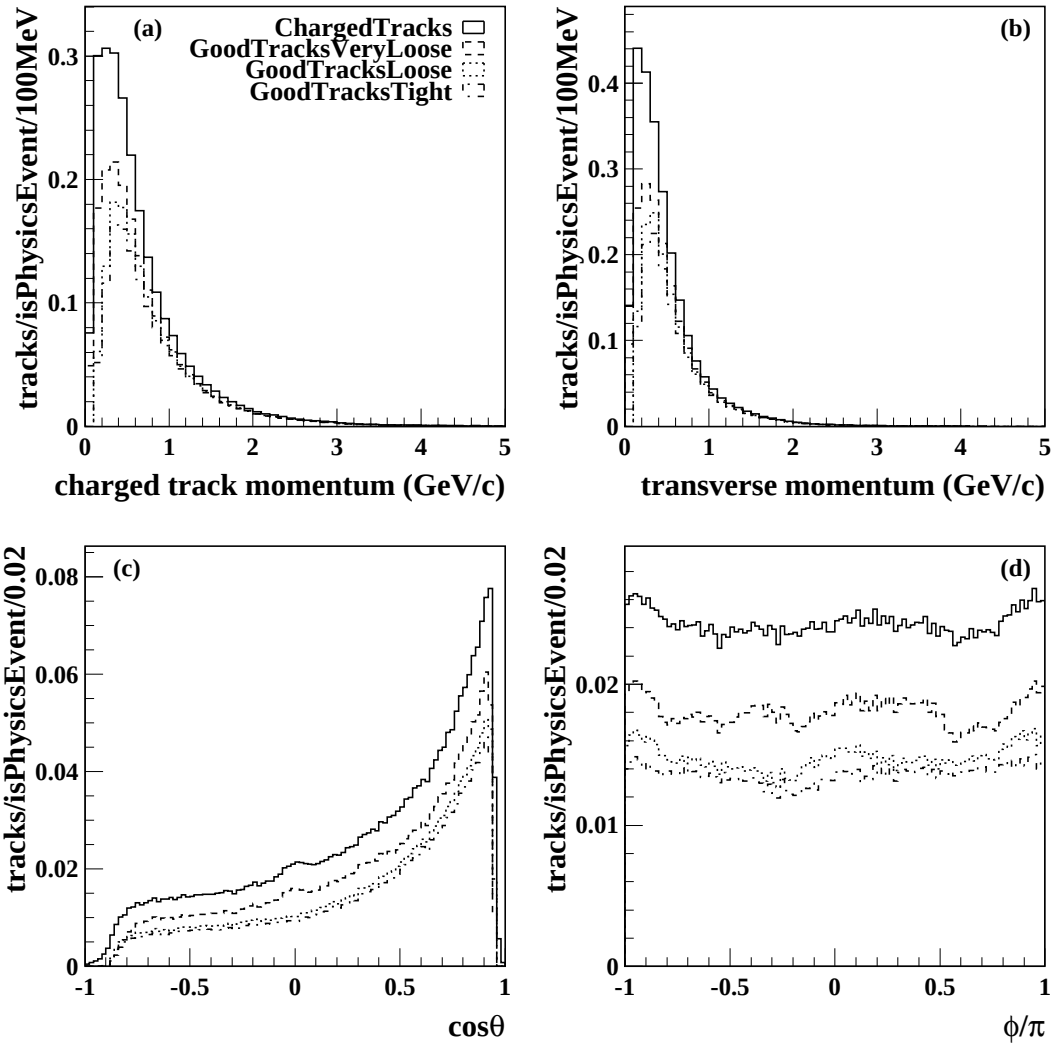

Figure 2: Distributions of (a) total momentum, (b) transverse momentum, (c) cosine of polar angle, and (d) azimuthal angle (all measured in the lab frame) for the charged track lists: *GoodTracks*, *GoodTracksVeryLoose*, *GoodTracksLoose*, *GoodTracksTight*. The plots are made from a typical run (number 12917) and normalized to display tracks/isPhysicsEvent/bin. The cut $R_2 < 0.45$ has been applied in these plots.

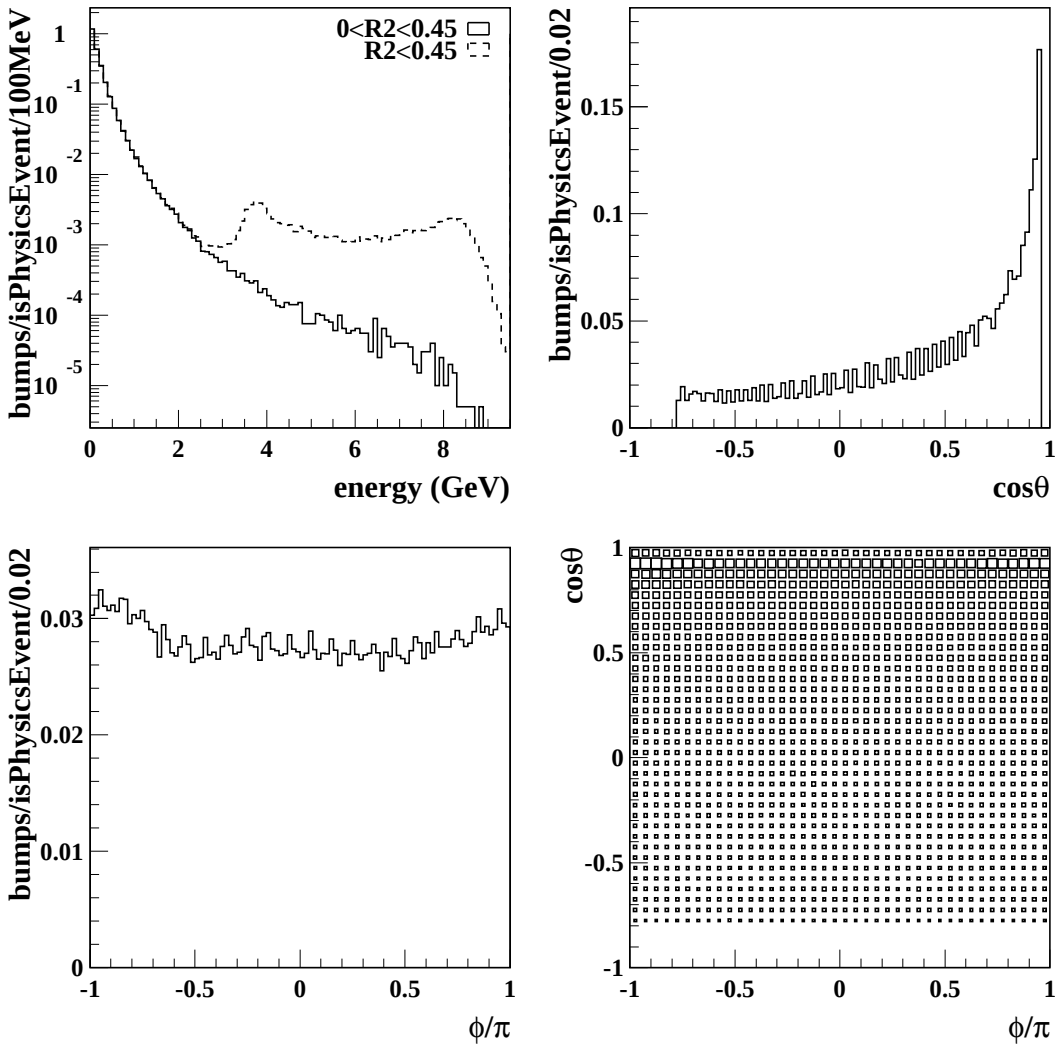

Figure 3: Distributions of (a) total energy, (b) cosine of polar angle, (c) azimuthal angles, and (d) a scatter plot of polar versus azimuthal angle for the neutral calorimeter bumps in the *CalorNeutral* list. The plots are made from a typical run (number 12917) and normalized to display bumps/isPhysicsEvent/bin. The cut $0 < R_2 < 0.45$ has been applied in these plots. The dashed histogram in (a) shows energy spectrum *without* excluding $R_2 = 0$.

2.2.2 Composition Lists

The composite particles used in this selection are: π^0, K^0_S, ρ^0, ρ^+, D^0, D^+, D^{*0} and D^{*+}. We identify candidates for each of these composites by combining entries in the reconstruction lists, and possibly other composite lists, and requiring that the resulting combinations pass loose kinematic cuts (applied to four-vector sums, without any refitting to include geometric or kinematic constraints). Table 5 summarizes the different decay modes represented by the composite lists used in this selection.

Decay Mode	Parent Mass [MeV/c^2]	Branching Ratio [%]
$D^{*+} \to D^0\pi^+$	2009.93	68.3%
$D^{*+} \to D^+\pi^0$		30.6%
$D^{*0} \to D^0\pi^0$	2006.7	61.9%
$D^{*0} \to D^0\gamma$		38.1%
$D^0 \to K^-\pi^+$	1864.51	3.91%
$D^0 \to K^-\pi^+\pi^0$		13.07%
$D^0 \to K^-\pi^+\pi^+\pi^-$		8.5%
$D^0 \to K^0_S\pi^+\pi^-$		2.7%
$D^+ \to K^-\pi^+\pi^+$	1869.3	9.0%
$D^+ \to K^0_S\pi^+$		1.45%
$\rho^+ \to \pi^+\pi^0$	770	100.0%
$\rho^0 \to \pi^+\pi^-$	770	100.0%
$K^0_S \to \pi^+\pi^-$	497.67	68.61%
$\pi^0 \to \gamma\gamma$	134.976	98.8%

Table 5: Decay modes represented in the composition lists which are used by this event selection. The mass values and branching ratios are those used in the Monte Carlo, which are consistent with Reference [1]. For the states which proceed via intermediate resonances ($D^0 \to K^-\pi^+\pi^0$, $D^0 \to K^0_S\pi^+\pi^-$, $D^0 \to K^-\pi^+\pi^+\pi^-$ and $D^+ \to K^-\pi^+\pi^+$) the branching ratios are summed over resonant and non-resonant contributions in the Monte Carlo, and include intermediate branching ratio factors for resonance decay into the final state shown in the table.

Pi0Loose and Pi0DefaultMass Lists

The π^0 candidates used in this selection are collected into a *pi0DefaultMass* list, which is refitted from a *pi0Loose* list with π^0 mass constraint. The *pi0Loose* list combines pairs of entries in the *CalorNeutral* list with:

1. both bumps having a minimum energy of 30 MeV, and the sum of their energies being at least 200 MeV,

2. a pair invariant mass in the range of 90–170 MeV/c^2, computed at the detector origin and assuming both entries are photons, and

3. both bumps having a lateral shower shape consistent with the expected pattern of energy deposits for an electromagnetic shower, as determined by a cut of LAT < 0.8.

Figure 4 shows the invariant mass and energy distribution for entries in the *pi0Loose* list and χ^2 probability of mass-constraint fit in *pi0DefaultMass* list for a typical run. The energy and momenta of π^0 candidates in this list are recalculated with a constraint on the π^0 mass (using the value in Table 5) calculated at the nominal per-run beam spot position. This refitting technique improves the energy resolution of the π^0 candidates from 3.0% to 2.5% [3]. About 80% of all π^0's produced in generic Monte Carlo have both photons within the calorimeter's geometrical acceptance[3]. The fraction of π^0's within the acceptance which are included in the *pi0DefaultMass* list varies with π^0 energy: it is 65-70% from 0.5–2.0 GeV, and then falls linearly down to 25% at about 5 GeV due to a large fraction of overlapping showers [3]. Thus, for the B decays studies reported here, we consider only π^0 candidates formed from separated clusters, since there are few merged pions in the the available kinematic range.

pi0SoftLoose List

Specially selected π^0 candidates are collected into a *pi0SoftLoose* list consisting of pairs of entries from the *CalorNeutral* list with:

- both bumps having a minimum energy of 30 MeV,
- a pair invariant mass in the range of 90–170 MeV/c^2, computed at the detector origin and assuming both entries are photons,
- both bumps having a lateral shower shape consistent with the expected pattern of energy deposits for an electromagnetic shower, as determined by a cut of LAT < 0.8, and
- the magnitude of the momentum sum of the pair is less than 450 MeV/c in the $\Upsilon(4S)$ frame.

KsLoose List

The K^0_S candidates used in this selection are collected into a *KsLoose* list consisting of pairs of *ChargedTrack* entries with an invariant mass (computed from the vertex for the two tracks obtained in one iteration of the VtxLeastChi2Vertex algorithm) in the range of 462–534 MeV/c^2. Figure 5 shows the invariant mass and energy distributions of K^0_S candidates in this list for a typical run. The average efficiency for K^0_S's produced in generic $B\overline{B}$ decays with momenta greater than ?? GeV/c to be selected in the *KsLoose* list is estimated to be ??% from Monte Carlo [2].

D0Default List

The D^0 candidates used in this selection are reconstructed in several modes (see Table 5) and collected into a single *D0Default* list. The following cuts are applied for each mode:

- $D^0 \to K^-\pi^+$: pairs of entries in the *GoodTracksLoose* list having an invariant mass within ± 45 MeV/c^2 of the nominal D^0 mass.

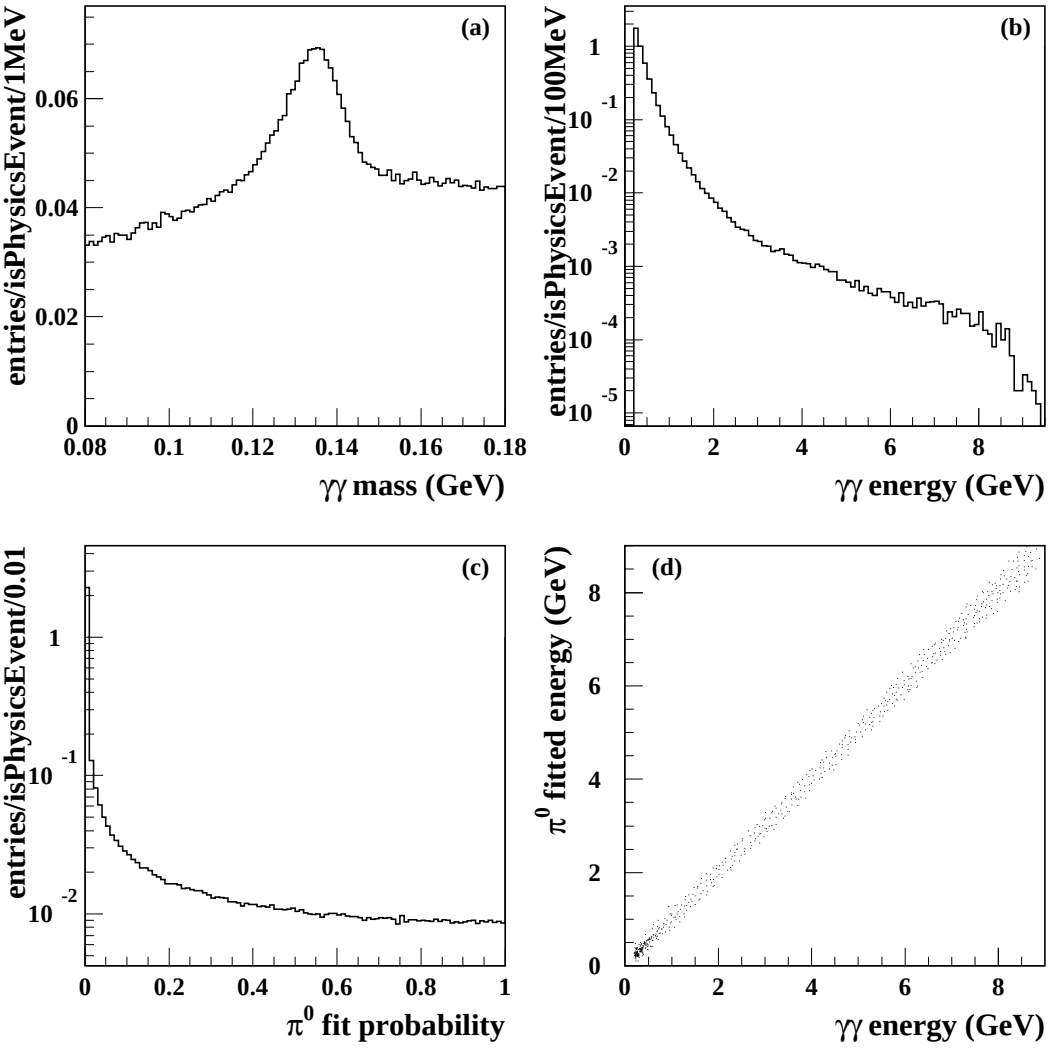

Figure 4: Distributions of (a) invariant mass, (b) total energy for pairs of neutral calorimeter clusters found in the *pi0Loose* list, (c) mass-constraint fit χ^2 probability in the *pi0DefaultMass* list, and (d) a scatter plot of energies comparison from a typical run (number 12917). The plots are normalized to show entries/isPhysicsEvent/bin.

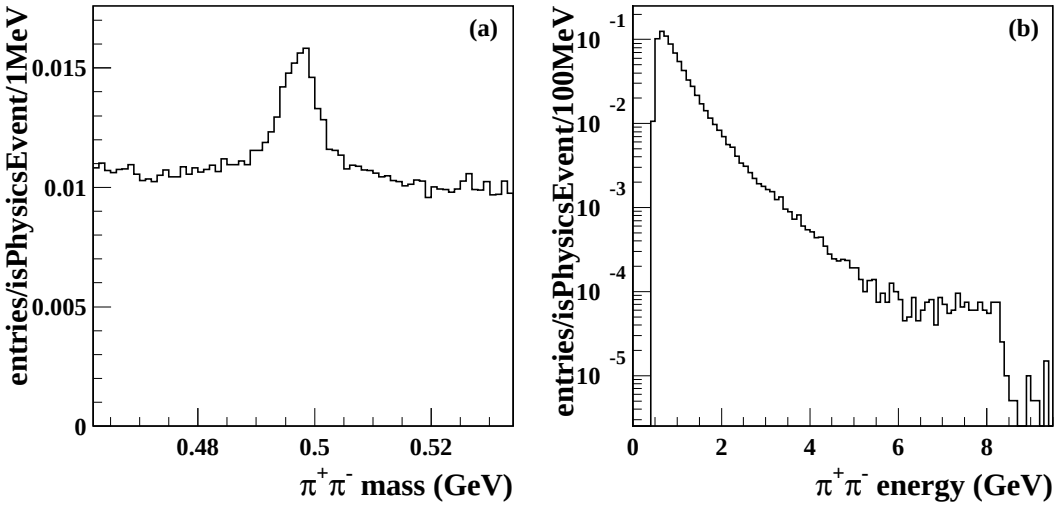

Figure 5: Distributions of (a) invariant mass and (b) total energy for pairs oppositely charged tracks found in the *ChargedTrack* list, from a typical run (number 12917). The plot are normalized to show entries/isPhysicsEvent/bin.

- $D^0 \to K^-\pi^+\pi^0$, $\pi^0 \to \gamma\gamma$: pairs of entries in the *GoodTracksLoose* list combined with an entry from the *pi0DefaultMass* list having an invariant mass within ± 80 MeV/c^2 of the nominal D^0 mass.
- $D^0 \to K^-\pi^+\pi^+\pi^-$: sets of four entries from the *GoodTracksVeryLoose* list with an invariant mass within ± 45 MeV of the nominal D^0 mass.
- $D^0 \to K^0_S\pi^+\pi^-$, $K^0_S \to \pi^+\pi^-$: pairs of entries in the *GoodTracksLoose* list combined with an entry from the *KSLoose* list having an invariant mass within ± 80 MeV/c^2 of the nominal D^0 mass.

In addition, all D^0 candidates must have momentum in the $\Upsilon(4S)$ frame greater than 1.3 GeV/c. All invariant masses are calculated with respect to the geometric vertex of the decay-product tracks. The nominal D^0 mass is given in Table 5. Figure 6 compares the invariant mass distributions measured in data for candidates reconstructed in each of these modes.

Figure 6: Invariant mass distributions of D^0 candidates in the *D0Default* list reconstructed as (a) $D^0 \to K^-\pi^+$, (b) $D^0 \to K^-\pi^+\pi^0$, $\pi^0 \to \gamma\gamma$, and (c) $D^0 \to K^-\pi^+\pi^+\pi^-$. The plots are generated from the ZZ subsample and normalized as decays/event/bin.

DcDefault List

The D^+ candidates used in this selection are reconstructed in several modes (see Table 5) and collected into a single *DcDefault* list. The following cuts are applied for each mode:

- $D^+ \to K^-\pi^+\pi^+$: three entries in the *GoodTracksLoose* list having an invariant mass within ± 45 MeV/c^2 of the nominal D^+ mass; and
- $D^+ \to K^0_S\pi^+$: an entry in the *KsLoose* list and combined with an entry in the *GoodTracksLoose* list having an invariant mass within ± 45 MeV/c^2 of the nominal D^+ mass.

In addition, all D^+ candidates must have momentum in the $\Upsilon(4S)$ frame greater than 1.3 GeV/c. All invariant masses are calculated with respect to the geometric vertex of the decay-product tracks. The nominal D^+ mass is given in Table 5.

DstarDefault List

D^{*+} candidates in the mode $D^0\pi^+$ are reconstructed as combinations of an entry in the *D0Default* list and an entry in the *GoodTracksVeryLoose* list ("soft pion"). Combinations passing the following cuts are added to a *DstarDefault* list:

- a maximum π^+ momentum of 450 MeV/c in the $\Upsilon(4S)$ frame,
- an invariant mass within 500 MeV/c^2 of the nominal D^{*+} mass (see Table 5), and
- a mass difference, $\Delta m \equiv m(D^0\pi^+) - m(D^0)$, in the range 130–160 MeV/c^2.
- 'right-sign' correlation between the charge of the soft pion and the kaon from the D^0 decay, where applicable

Dstar0Default List

D^{*0} candidates in the mode $D^0\pi^0$ are reconstructed as combinations of an entry in the *D0Default* list and an entry in the *pi0SoftLoose* list ("soft pion"). Combinations passing the following cuts are added to a *Dstar0Default* list:

- π^0 momentum less than 450 MeV/c in the $\Upsilon(4S)$ frame
- an invariant mass within 500 MeV/c^2 of the nominal D^{*0} mass (see Table 5), and
- a mass difference, $\Delta m \equiv m(D^0\pi^0) - m(D^0)$, in the range 130–160 MeV/c^2.

D^{*0} candidates in the mode $D^0\gamma$ are reconstructed as combinations of an entry in the *D0Default* list and an entry in the *CalorNeutral* list. Combinations passing the following cuts are added to a *Dstar0Default* list:

- photon lab energy greater than 100 MeV, and less than 450 MeV in the $\Upsilon(4S)$ frame
- an invariant mass within 500 MeV/c^2 of the nominal D^{*0} mass (see Table 5), and
- a mass difference, $\Delta m \equiv m(D^0\pi^0) - m(D^0)$, in the range 120–170 MeV/c^2.

rho Lists

Oppositely charged tracks from the *GoodTracksLoose* list that lie within ± 160 MeV/c^2 of the nominal ρ^0 mass are collected on the *rho0Default* list. The ρ^+ list *rhoCDefault* is a

collection formed from paired entries on the *GoodTracksLoose* and *pi0DefaultMass* lists lying within ± 160 MeV/c^2 of the nominal ρ^+ mass.

a1CDefault List

Candidates for $a_1^+ \to \rho^0\pi^+$ are collected on the *a1CDefault* list, by combining entries from the *rho0Default* and *GoodTracksLoose* lists. An invariant mass between 1.0 and 1.6 GeV/c^2 is required.

2.2.3 B^0 and B^+ Skims

Decay Mode	Branching Ratio [10^{-3}]
$B^0 \to D^{*-}\pi^+$	2.7
$B^0 \to D^{*-}\rho^+$	7.0
$B^0 \to D^{*-}a_1^+$	12.2
$B^0 \to D^-\pi^+$	3.0
$B^0 \to D^-\rho^+$	8.2
$B^0 \to D^-a_1^+$	6.0
$B^+ \to \overline{D}^{*0}\pi^+$	5.0
$B^+ \to \overline{D}^{*0}\rho^+$	14.7
$B^+ \to \overline{D}^{*0}a_1^+$	18.3
$B^+ \to \overline{D}^0\pi^+$	4.8
$B^+ \to \overline{D}^0\rho^+$	13.2
$B^+ \to \overline{D}^0a_1^+$	4.2

Table 6: B decay modes represented in the composition lists which are used by this event selection. The branching ratios are those used in the Monte Carlo, which are consistent with Reference [1].

Common lists are constructed, *B0ToDDtsarDefault* for neutral B's and *BchToDDstarDefault* for charged B's, using the decay modes listed in Table reftable:Bmodes, for pairs of entries from the *DstarDefault*, *DcDefault*, *D0Default*, or *Dstar0Default* lists and the *GoodTracksloose*, *rhoCDefault*, or *a1CDefault* lists, with the following additional requirements on the B candidate:

- the energy-substituted mass lies in the range 5.15 to 5.35 GeV/c^2, and
- the reconstructed energy lies within ± 300 MeV of one-half the center-the-mass energy.

A total of 64 separate tag bits are defined for each of the complete B decay chains. The final pre-selected datasets are based on the two composition lists, *B0ToDDstarDefault* and *BchDdstarDefault*, which are used as the basis for the *allB0Tight* and *allBchTight* skims respectively.

2.2.4 Ntuple Production

Ntuples for analysis are produced by running the *BrecoUser* program, reading events flagged with the *allB0Tight* or *allBchTight* tag bit from a corresponding skim. Table 7 summarizes the software versions that were used. The composition lists created when the tag bits is set are not stored in the event, so the ntuple creation job must recreate them. At this stage, various vertex fits are performed, to create the ntuple output variables:

- In selecting D^0 and D^+ candidates for B reconstruction, a single iteration vertex constraint fit using GeoKin; in reconstructing the B parent, a combined mass and vertex constraint fit using GeoKin is applied to the D^0 and D^+;
- All $D^{*+} \to D^0\pi^+$ candidates are refitted with the beam-spot constraint to improve the soft pion angle measurement, using a fixed vertical beam spot sigma of 45 μm; and
- A vertex fit using GeoKin is applied to the final B candidate.

Package	Version Tag
BrecoUser	fmv051400
CompositionTools	fmv051300
CompositionSequences	fmv051300c
VtxFitter	V00-01-37

Table 7: Versions of the main packages used to create the Elba sample ntuples. Most other packages used the versions in the *analysis-1* release.

3 Reconstruction of B Mesons

The final B reconstruction studies discussed in this report are based on the ntuples created from the skimmed samples *allB0Tight* and *allBchTight*. As described in section 2.2, the composition lists are used to select the candidates and to generate the variables contained in the skimmed ntuples. The final analysis uses only a subset of the 64 possible decay chains and frequently makes tighter final cuts. We will repeat here, in a physics language more appropriate for a final presentation, the selection requirements for the B decay modes included in this study. A tabular summary of the final cuts is also provided, organized in a way to show a comparison with the pre-selection cuts. If the 'Final Analysis' column is blank in these comparisons, the cut is identical to the pre-selection. The additional cuts in the final selection are aimed at producing a result with a signal purity of around 90%, although further optimization in this direction is still required.

3.1 Track Selection

For most charged particles, we require the reconstructed track satisfy a minimal quality selection (*GoodTracksLoose* list). In order to reduce contributions from beam gas and beam

wall backgrounds, tracks are required to satisfy a loose requirement of having a distance of closest approach within ± 10 cm in z and 1.5 cm in radius of the average beam spot position. The beam spot position is determined on a run-by-run basis. The transverse momentum is required to lie between 0.1 and 10 GeV/c. Finally, the particle is required to have penetrated the drift chamber, with at least 20 assigned hits. In the case of the soft pion from the transition $D^{*+} \to D^0\pi^+$ or the daughters from a K^0_S decay (discussed below), these restrictions are removed, and any charged track is used (*ChargedTrack* list) in the reconstruction.

Criteria	Skim	Final Analysis
Default Track	*GoodTrackLoose*	
p_T	[0.1,10.] MeV/c	
d_0	< 1.5 cm	
z_0	$< 10.$ cm	
n_{DCH}	> 20	
Soft Track	*ChargedTrack*	
No cuts		

Table 8: Summary of cuts for charge tracks (*GoodTracksLoose* and *ChargedTracks* list)

3.2 Particle Identification

The SMS particle selector is used to identify kaons in D^0 and D^+ reconstruction. It permits to reject pions background in modes where it is needed to obtain a rough optimization of $S^2/(S+B)$. [3]

All selectors use likelihoods calculated with information given by these three subdetectors:

- *Silicon Vertex Detector*: measurement of dE/dX and the number of hits,
- *Drift Chamber*: measurement of dE/dX and the number of hits,
- *DIRC*: value of the Cerenkov angle and the number of photons.

In B reconstruction to exclusive modes, two particular selectors are used:

- The SMS "Not A Pion" selector is used most of the time. For this selection, if a subdetector gives no information, the particle is assumed to be a kaon for this detector.
- The SMS "Tight" selector is used for modes with higher backgrounds such as $B^- \to D^{*0}\pi^-$, $D^0 \to K^-\pi^+\pi^0$ or $D^0 \to K^-\pi^+\pi^-\pi^+$. This algorithm requires that the likelihood calculated for the kaon hypothesis be greater than the pion and proton hypotheses. The effect of this selection on the decay mode $B^+ \to \overline{D}^{*0}\pi^+$, $D^0 \to K^-\pi^+\pi^0$ can be seen in Fig. 7.

[3] A detailed optimization study is in progress.

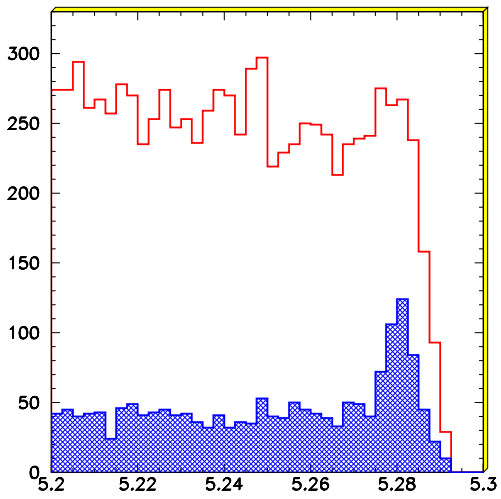

Figure 7: Effect of SMS "Tight" Selector on the reconstruction of the decay mode $B^- \to D^{*0}\pi^-$, $D^0 \to K^-\pi^+\pi^0$. Blank histogram: without any selection; colored histogram: SMS "Tight" selection required for the kaon in the decay $D^0 \to K^-\pi^+\pi^0$

3.3 π^0 Reconstruction

The π^0 are formed by combining pairs of photon candidates taken from the *CalorNeutral* list. The photon energy threshold is set at 30 MeV and a cut LAT < 0.8 is applied to reject the background. The reconstructed $\gamma\gamma$ mass is shown in Fig.8. The invariant mass of the photon pair is required to be within ± 20 MeV/c^2 of the nominal π^0 mass. For those π^0 mesons produced by $\rho^+ \to \pi^+\pi^0$ or $D^0 \to K^-\pi^+\pi^0$, an additionnal cut, $E > 200$ MeV, is applied to the π^0 energy. For the π^0 from $D^{*0} \to D^0\pi^0$, the π^0 is required to have momentum less than 450 MeV/c in the $\Upsilon(4S)$ frame. The selection efficiency, determined from generic $B\overline{B}$ events in SP3 Monte Carlo, increases from about 40% at threshold to 55% for π^0's with 2 GeV in energy. The variation in efficiency as a function of the π^0 energy is shown on Fig. 8.

Criteria	Skim	Final Analysis
Default π^0	*pi0DefaultMass*	
$E(\gamma)$	> 30 MeV	
$E(\gamma\gamma)$	> 200 MeV	
LAT	< 0.8	
$m(\gamma\gamma)$	[90.,170.] MeV/c^2	[115.,155.] MeV/c^2
Soft π^0	*pi0SoftLoose*	
$E^*(\gamma\gamma)$	< 450 MeV/c	

Table 9: Summary of cuts for π^0 selection (*pi0DefaultMass* and *pi0SoftLoose* lists)

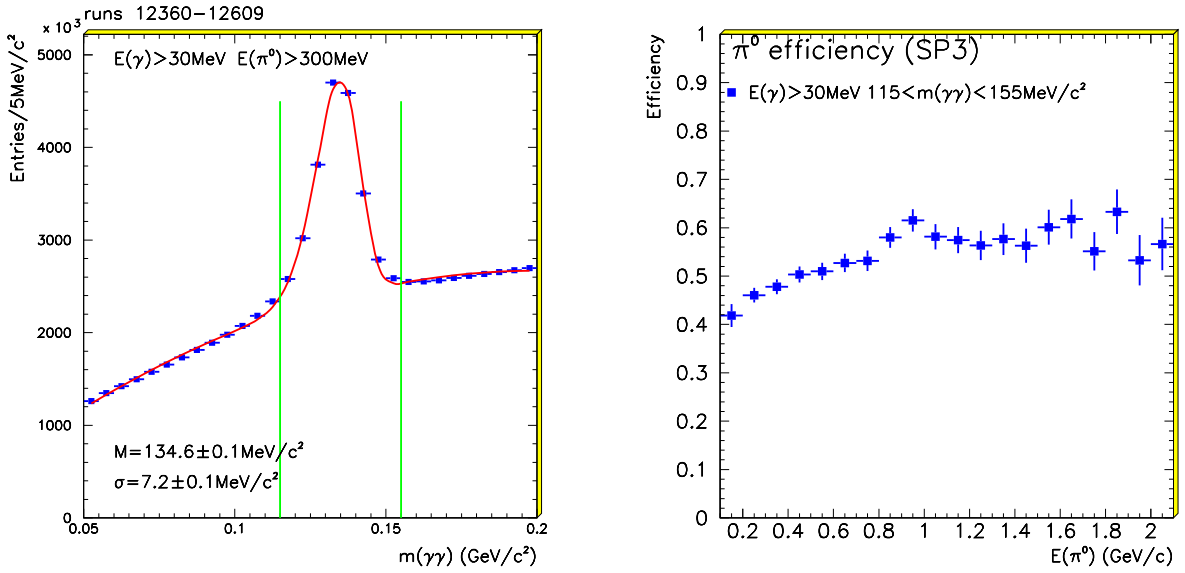

Figure 8: The $\gamma\gamma$ mass distribution in the data for $E(\pi^0) > 300$ MeV is shown on the left. The data points are overlaid with the result of a fit using a Novosibirsk function for the signal plus a 2^{nd}-order polynomial for the background. The vertical lines indicate the mass window used to select π^0 candidates. The π^0 selection efficiency as a function of the π^0 energy in shown on the right for generic $B\overline{B}$ events in the SP3 Monte Carlo.

3.4 K^0_S Reconstruction

The K^0_S candidates are formed from pairs of oppositely charged tracks without restrictions on p_T or distance of closest approach to the beam spot centroid (*ChargedTrack* list). A vertex fit is performed using GeoKin, where a χ^2 probability greater than 0.1% is required. The invariant mass computed at this vertex location is required to lie in with ± 36 MeV/c^2 of the nominal K^0_S mass. The opening angle, α, between the flight directionand the momentum vector for the K^0_S candidate must be smaller than 200 mr. Finally, the transverse flight distance from the primary vertex in the event, r_{xy}, is required to be greater than 2 mm. The $\pi^+\pi^-$ mass distribution for candidates passing these requirements is shown in Figure 9. The fitted mass is zzz, consistent with the nominal value. The resolution is observed to be zzz, in agreement with Monte Carlo estimates of zzz. The efficiency for a K^0_S to satisfy these requirements is shown in Figure 9. A mass constraint fit is applied to those K^0_S candidates passing these requirements, for use in subsequent reconstruction of charm mesons.

3.5 Charm Meson Reconstruction

D^0 Candidates

D^0 candidates are reconstructed in the modes $D^0 \to K^-\pi^+$, $D^0 \to K^-\pi^+\pi^0$, $D^0 \to K^-\pi^+\pi^-\pi^+$, and $D^0 \to K^0_S\pi^+\pi^-$. We require that the daughter tracks used in the $D^0 \to K^-\pi^+$ mode have a minumum momentum of 200 MeV/c. For $D^0 \to K^-\pi^+\pi^0$ $D^0 \to$

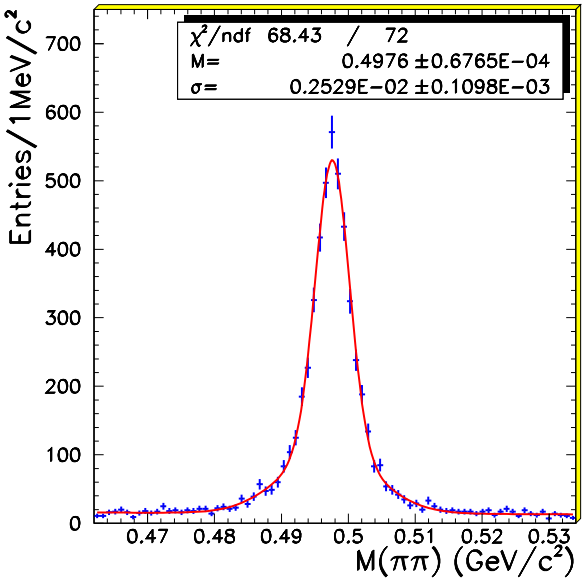

Figure 9: Distribution of $\pi^+\pi^-$ invariant mass for K^0_S candidates, after cuts on the flight angle α and the transverse flight distance.

Criteria	Skim	Final Analysis
Default K^0_S	*KsLoose*	
Vertex Fitter	VtxLeastChi2Vertex	GeoKin
$m(\pi^+\pi^-)$	$m(K^0_S) \pm 36$ MeV/c^2	
χ^2		> 0.001
α		< 300 mr
r_{xy}		> 2 mm

Table 10: Summary of cuts for K^0_S selection (*KsLoose* list)

$K^-\pi^+\pi^-\pi^+$, and $D^0 \to K^0_S\pi^+\pi^-$ modes in channels other than $\overline{B}^0 \to D^{*+}\pi^-$ and $D^{*+}\rho^-$, the minimum charged track momentum is 150 MeV/c. Also, in these modes, we use the SMS "Not A Pion" particle selector to reject pion backgrounds for the kaon track in modes where background rejection is needed to obtain a rough optimization of $S^2/(S+B)$. D^0 candidates in the channels $\overline{B}^0 \to D^{*+}\pi^-$ and $D^{*+}\rho^-$ are required to have an invariant mass within $\pm 2.5\sigma$ of the fitted D^0 mass in the inclusive D^0 spectrum (Table 12) in the B candidate sample. In all other cases, the D^0 candidates are required to lie within $\pm 3\sigma$, calculated on an event-per-event basis, of the nominal D^0 mass. For $D^0 \to K^-\pi^+\pi^0$ mode, we only reconstruct the dominant resonant mode $D^0 \to K^-\rho^+$, $\rho^+ \to \pi^+\pi^0$ at this moment. This, the $\pi^+\pi^0$ invariant mass is required to lie within ± 150 MeV/c^2 of the nominal ρ mass and the angle between the π^+ and K^- in the $\pi^+\pi^0$ rest frame, $\theta^*_{K\pi}$, must satisfy $|\cos\theta^*_{K\pi}| > 0.4$. However, this choice of cuts is not optimal, which would require maximizing $S^2/(S+B)$ based on the Dalitz distribution [13, 14]. All D^0 candidates must have momentum greater

than 1.3 GeV/c in the $\Upsilon(4S)$ frame. A vertex fit is performed using GeoKin, where a χ^2 probability greater than 0.1% is required.

Criteria	Skim	Final Analysis
Default D^0	*D0Default*	
Vertex Fitter	GeoKin	GeoKin
χ^2		> 0.001
$p^*(D^0)$	> 1.3 GeV/c	
$D^0 \to K^-\pi^+$		
$m(K^-\pi^+)$	$m(D^0) \pm 45$ MeV/c^2	± 18 MeV/c^2
$p(K^-)$	> 100 MeV/c	> 200 MeV/c
$p(\pi^+)$	> 100 MeV/c	$> 200^\dagger$ MeV/c^2
$D^0 \to K^-\pi^+\pi^0$		
$m(K^-\pi^+\pi^0)$	$m(D^0) \pm 80$ MeV/c^2	± 33.5 MeV/c^2
$p(K^-, \pi^\pm)$	> 100 MeV/c	> 150 MeV/c
$m(\pi^+\pi^0)$		$m(\rho) \pm 150$ MeV/c^2
$\lvert\cos\theta^*_{K\pi}\rvert$		> 0.4
$D^0 \to K^0_S\pi^+\pi^-$		
$m(K^0_S\pi^+\pi^-)$	$m(D^0) \pm 80$ MeV/c^2	± 33.5 MeV/c^2
$p(\pi^\pm)$	> 100 MeV/c	> 150 MeV/c
$D^0 \to K^-\pi^+\pi^+\pi^-$		
$m(K^-\pi^+\pi^+\pi^-)$	$m(D^0) \pm 45$ MeV/c^2	± 17 MeV/c^2
$p(K^-, \pi^\pm)$	> 100 MeV/c	> 150 MeV/c

† For modes other than $\overline{B}^0 \to D^{*+}\pi^-$ or $D^{*+}\rho^-$

Table 11: Summary of cuts for D^0 selection (*D0Default* list)

Mode	m_D (MeV/c^2)	σ_{m_D} (MeV/c^2)
$D^0 \to K^-\pi^+$	1863.1 ± 0.5	6.8 ± 0.6
$D^0 \to K^-\pi^+\pi^0$	1863.1 ± 1.4	11.5 ± 1.4
$D^0 \to K_s\pi^-\pi^+$	1863.3 ± 1.0	8.1 ± 1.0
$D^0 \to K^-\pi^+\pi^-\pi^+$	1863.7 ± 0.5	6.2 ± 0.8

Table 12: D^0 fitted mass and widths.

D^+ Candidates

D^+ candidates are reconstructed in the modes $D^+ \to K^-\pi^+\pi^+$ and $D^+ \to K^0_S\pi^+$. We require that the kaon used in the $K^-\pi^+\pi^+$ mode have a minumum momentum of 200 MeV/c; the pions are required to have momentum greater than 150 MeV/c. For the $K^0_S\pi^+$ mode, the minimum charged track momentum is 200 MeV/c. We also use the SMS "Not A Pion" particle selector to reject pion backgrounds for the kaon track in modes where background rejection is needed to obtain a rough optimization of $S^2/(S+B)$. D^+ candidates are required

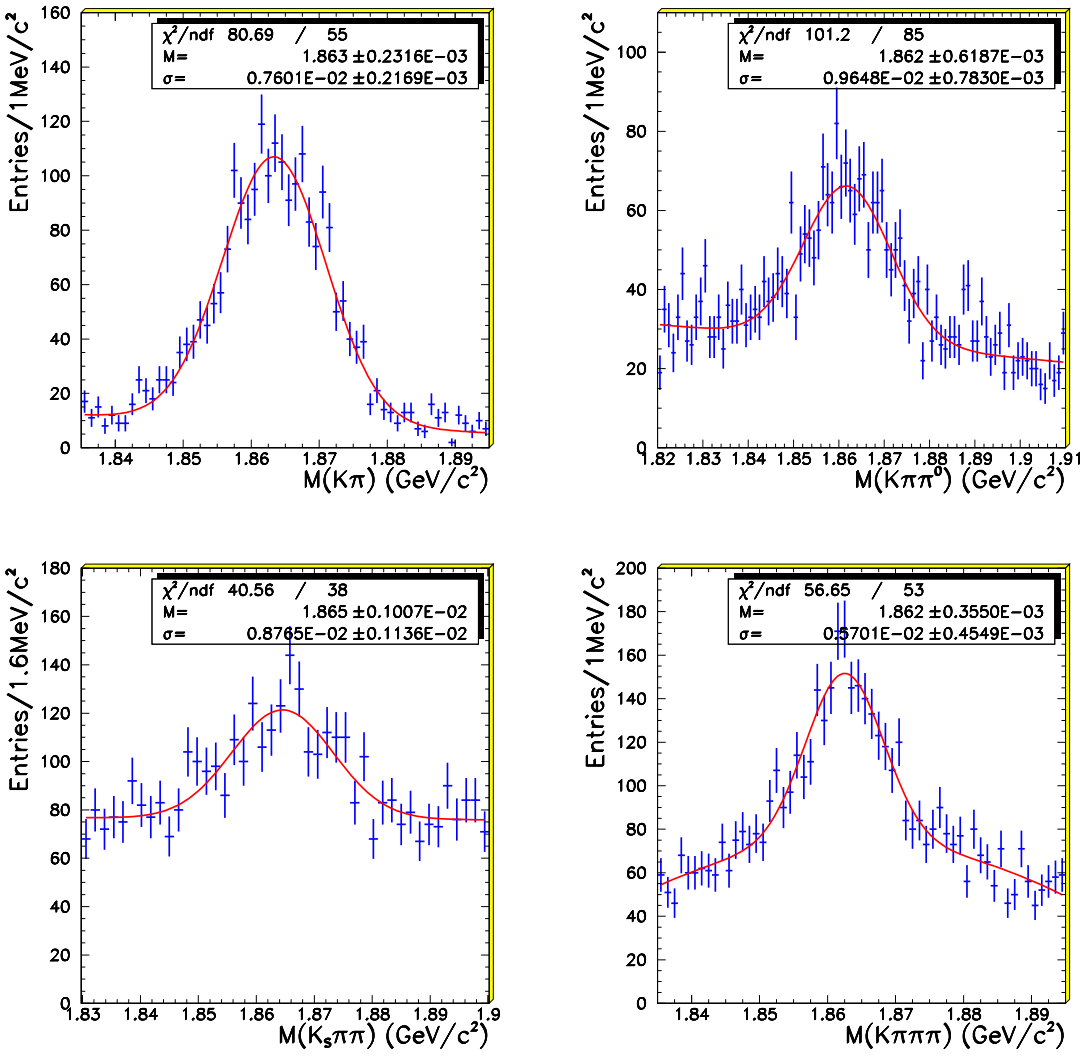

Figure 10: D^0 candidates selected for $D^0 \to K^-\pi^+$, $D^0 \to K^-\pi^+\pi^0$ $D^0 \to K^0_S\pi^+\pi^-$, and $D^0 \to K^-\pi^+\pi^-\pi^+$ modes in the AllB0Tight ntuples.

to have an invariant mass within $\pm 3\sigma$, calculated on an event-by-event basis, of the nominal D^+ mass. All D^+ candidates must have momentum greater than 1.3 GeV/c in the $\Upsilon(4S)$ frame. A vertex fit is performed using GeoKin, where a χ^2 probability greater than 0.1% is required.

Criteria	Skim	Final Analysis
Default D^+	*DchDefault*	
Vertex Fitter	GeoKin	GeoKin
χ^2		> 0.001
$p^*(D^+)$	> 1.3 GeV/c	
$D^+ \to K^-\pi^+\pi^+$		
$m(K^-\pi^+\pi^+)$	$m(D^+) \pm 45$ MeV/c^2	$\pm 3\sigma^\dagger$
$p(K^-)$	> 100 MeV/c	> 200 MeV/c
$p(\pi^+)$	> 100 MeV/c	> 150 MeV/c
$D^+ \to K^0_S\pi^+$		
$m(K^0_S\pi^+)$	$m(D^0) \pm 45$ MeV/c^2	$\pm 3\sigma^\dagger$
$p(\pi^+)$	> 100 MeV/c	> 200 MeV/c

† Calculated on an event-by-event basis

Table 13: Summary of cuts for D^+ selection (*DchDefault* list)

D^{*+} Candidates

We form D^{*+} candidates by combining the a D^0 with a pion which has momentum greater than 70 MeV/c. GeoKin is used to perform a vertex fit for the D^{*+} using the constraint of the beam spot to improve the angular resolution for the soft pion. A fixed $\sigma = 40$ μm is used to model the beam spot spread in the vertical direction. The fit is required to converge, but no cut is applied on the proability of χ^2. After fitting, selected D^{*+} candidates are required have Δm within $\pm 2.5\sigma$ of the measured nominal value. The width is taken to be a weighted average of the core and broad Gaussian distributions required to fit the Δm distribution.

D^{*+} candidates are also formed by combining the a D^+ with a π^0. The maximum momentum of the π^0 in the $\Upsilon(4S)$ frame is 450 MeV/c. The D^{*+} candidates are required have Δm within $\pm 2.5\sigma$ of the nominal mass-difference value.

Criteria	Skim	Final Analysis
Default D^{*+}	*DstarDefault*	
$D^{*+} \to D^+\pi^-$		
Vertex Fitter		GeoKin
χ^2	convergence	
$m(D^0\pi^+) - m(D^0)$	[130,160] MeV/c^2	$\pm 2.5\sigma$ MeV/c^2
$p^*(\pi^+)$	[70,450] MeV/c	

Table 14: Summary of cuts for D^{*+} selection (*DstarDefault* list)

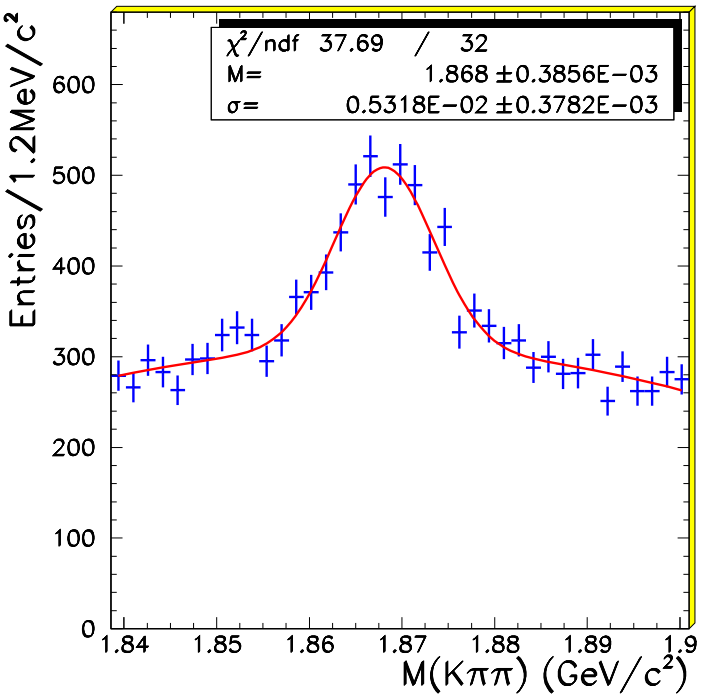

Figure 11: $D^+ \to K^-\pi^+\pi^+$ candidates selected for in the AllB0Tight and AllBchTight ntuples.

D^{*0} Candidates

D^{*0} candidates are reconstructed by combining a selected D^0 with a π^0 having momentum less than 450 MeV/c in the $\Upsilon(4S)$ frame. Selected D^{*0} candidates are required to have Δm within 4 MeV/c^2 of the nominal value. The Δm distribution, obtained from an inclusive sample of $D^0 \to K^-\pi^+$ decays, is shown in Fig. 14, for both a $b\overline{b}$ enriched ($p^*(D^0) < 2.5$ GeV/c) and a $c\overline{c}$ enriched sample ($p^*(D^0) > 2.5$ GeV/c).

Criteria	Skim	Final Analysis
Default D^{*+}	*Dstar0Default*	
$D^{*0} \to D^0\pi^0$		
$m(D^0\pi^0) - m(D^0)$	[130,160] MeV/c^2	± 4 MeV/c^2
$p^*(\pi^0)$	[70,450] MeV/c	
$D^{*0} \to D^0\gamma$		
$m(D^0\gamma) - m(D^0)$	[120,170] MeV/c^2	[130.,150.] MeV/c^2

Table 15: Summary of cuts for D^{*0} selection (*Dstar0Default* list)

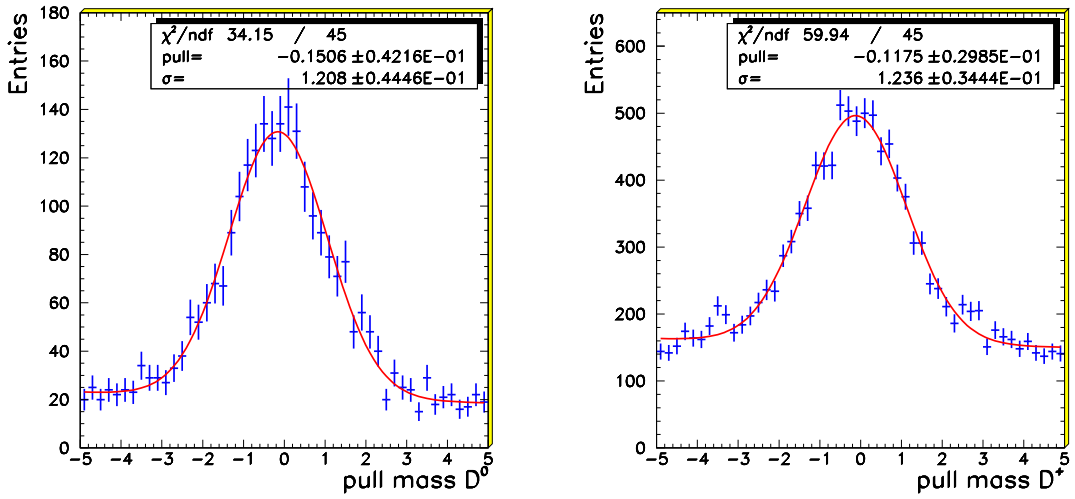

Figure 12: Pull distributions in mass for candidates in the modes $D^0 \to K^-\pi^+$ (left) and $D^+ \to K^-\pi^+\pi^+$ (right).

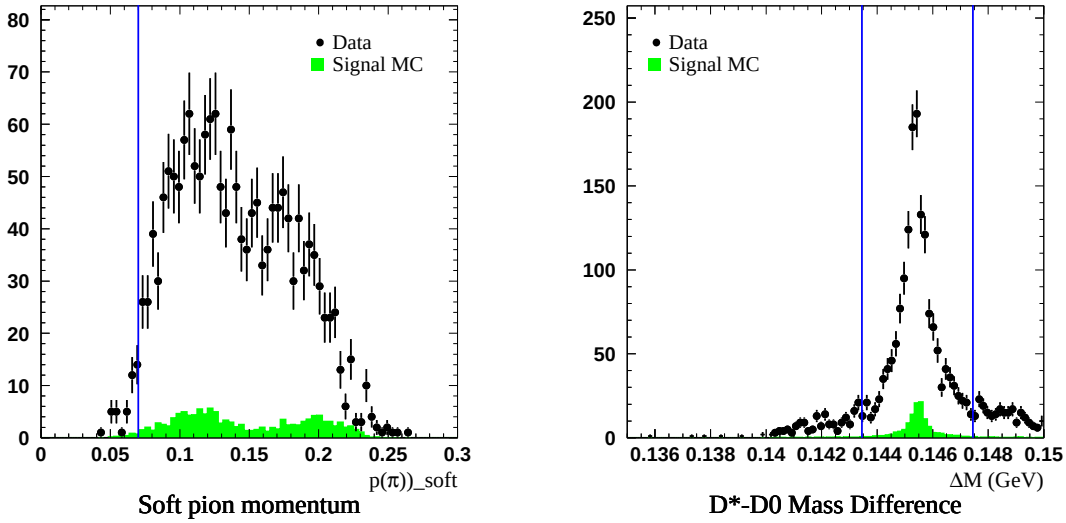

Figure 13: Distribution of soft pion momentum in the $\Upsilon(4S)$ frame (left) and $m(D^{*+}\pi^-) - m(D^0)$ mass distribution for D^{*+} candidates in the $\overline{B}^0 \to D^{*+}\pi^-$, $D^0 \to K^-\pi^+$ mode. Data includes selected D^{*+} candidates for all modes included in the B0toDStarX ntuples. Units in both plots are GeV. Vertical lines indicate selection criteria

3.6 B Candidate Selection

B meson candidates are obtained by combining a D or D^* candidate, reconstructed as described in section 3.5, with a π, ρ or a_1 meson.

The pion momentum spectrum for the two-body decay $\overline{B}^0 \to D^{*+}\pi^-$ is shown in Fig. 15

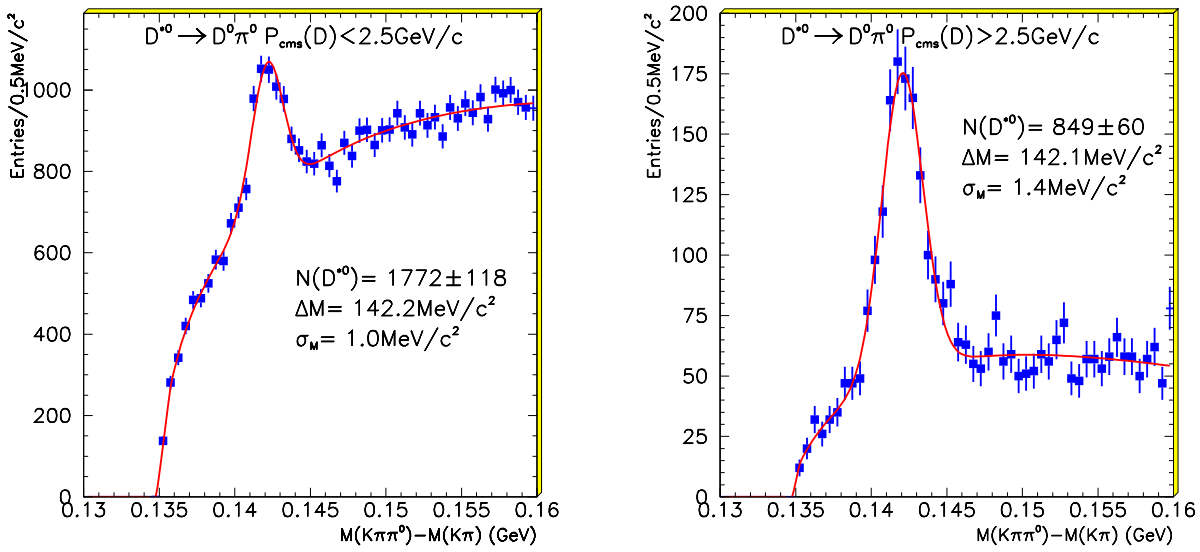

Figure 14: Δm distribution for $D^{*0} \to D^0\pi^0$ decays, where $p^*(D^0) < 2.5$ GeV/c (left) and $p^*(D^0) > 2.5$ GeV/c(right)

Mode	Δm (MeV/c^2)	$\sigma_{\Delta m}$ (MeV/c^2)
$D^{*+} \to D^0\pi^+$		
$D^0 \to K^-\pi^+$	145.45	0.8
$D^0 \to K^-\pi^+\pi^0$	145.54	1.1
$D^0 \to K^0_S\pi^+\pi^-$	145.45	0.9
$D^0 \to K^-\pi^+\pi^+\pi^-$	145.54	0.8
$D^{*0} \to D^0\pi^0$	142.2	1.0
$D^{*0} \to D^0\gamma$	142.2	5.2

Table 16: Δm signal widths used for D^* candidate selection.

For this analysis, the pion is required to have momentum greater than 500 MeV/c. No particle identification requirement is made for this track.

For the $\overline{B}^0 \to D^{*+}\rho^-$ mode, ρ^+ candidates are formed by combining a π^0 meson and a charged pion both with momentum greater than 200 MeV/c. We require the ρ momentum to be greater than 1 GeV/c, and the $\pi^-\pi^0$ invariant mass to satisfy $|m(\pi^-\pi^0) - 770| < 150$ MeV/c^2. For the $\overline{B}^0 \to D^{*+}a_1^-$ mode, the a_1^- meson is selected by combining three charged pions, where the invariant mass must lie in the range 1.0 to 1.6 MeV/c^2. In addition, a vertex constraint fit to the a_1^- candidate is required to converge with $\chi^2 > 0.1\%$.

In the case of a correctly reconstructed B meson produced by the decay of an $\Upsilon(4S)$, within the experimental resolution, the measured sum of neutral and charged energies, E^*_{meas}, must be equal to the beam energy, E^*_{beam}, both evaluated in the $\Upsilon(4S)$ frame. We define

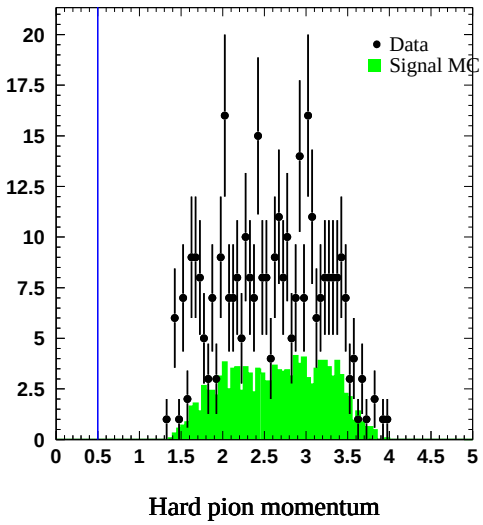

Figure 15: Spectrum of pion momentum in the two-body decay $\overline{B}^0 \to D^{*+}\pi^-$. The vertical line indicates the cut value.

ΔE to be the difference between the measured B candidate energy and beam energy in the $\Upsilon(4S)$ frame as:[5]

$$\Delta E \quad = \quad E^*_{meas} - E^*_{beam} \tag{1}$$

The resolution on $\sigma_{\Delta E}$ varies from 20 to 40 MeV depending on mode. The list of the modes we have studied and the corresponding values of $\sigma_{\Delta E}$ are given in Tables 18 and 20.

We define an energy substituted B mass, m_{ES}, as:

$$m^2_{ES} \quad = \quad (E^*_{beam})^2 - \left(\sum_i \vec{p}_i\right)^2 \tag{2}$$

where the $\vec{p}_i$ is the momentum of the ith daughter of the B candidate. The predicted resolution in m_{ES} is typically about 2.6 MeV/c^2 for most decay modes involving all-charged final states. This is about a factor of 10 better than the resolution in the reconstructed invariant mass. The resolution for m_{ES} is dominated by the beam energy spread rather than by the detector resolution, although there are examples where the measurement errors can contribute as well. It is largely uncorrelated with the error on ΔE [8].

The variables ΔE and m_{ES} are used to define a signal region and sidebands for background study. For all modes, the region between 5.2 and 5.3 GeV/c^2 in m_{ES} and between $\pm$300 MeV in ΔE is used to study the B candidates. The peak position, m_B, which should be the nominal B mass, and the resolution $\sigma_{m_{ES}}$ are extracted from the distribution of m_{ES} after requiring ΔE be consistent with zero to within $\pm 2.5\sigma$. The resolution in ΔE is extracted from the ΔE distribution obtained by requiring m_{ES} lie within $\pm 2.5\sigma_{m_{ES}}$ of m^0_B.

The signal region in the two dimensional plane m_{ES} versus ΔE is defined as a area $\pm 2.5\sigma$ wide centered at the nominal B mass, m^0_B, and $\Delta E = 0$. The sidebands outside this signal

region are currently under study, both to demonstrate the appropriateness of our assumed background form and to better understand feeddown from other channels.

We allow only one candidate per event to appear in the m_{ES} versus ΔE distribution. Several different ways to choose the best candidate from among multiple candidates in the same event have been explored. The criteria selected in the end is to consider only the entry with the smallest absolute value for ΔE.

3.7 Background Rejection

The background composition in our signal region has significant contributions from both other $B\overline{B}$ events and continuum, and depends on the decay mode. In $\overline{B}^0 \to D^{*+}\pi^-$, for example, a study of 2 fb^{-1} of generic $B\overline{B}$ shows the most significant background to be from $c\overline{c}$ events.

To enrich the final sample with B signal and obtain a rough optimization of signal to background [4], we use two event shape techniques to reduce continuum background.

First, each event is required to satisfy $R_2 < 0.5$ where R_2 is the ratio of the second Fox-Wolfram moment to the zeroth moment determined using charged tracks and unmatched neutral showers in the $\Upsilon(4S)$ frame. This is designed to reject the jetlike continuum events over the more uniformly distributed $\Upsilon(4S)$ decays.

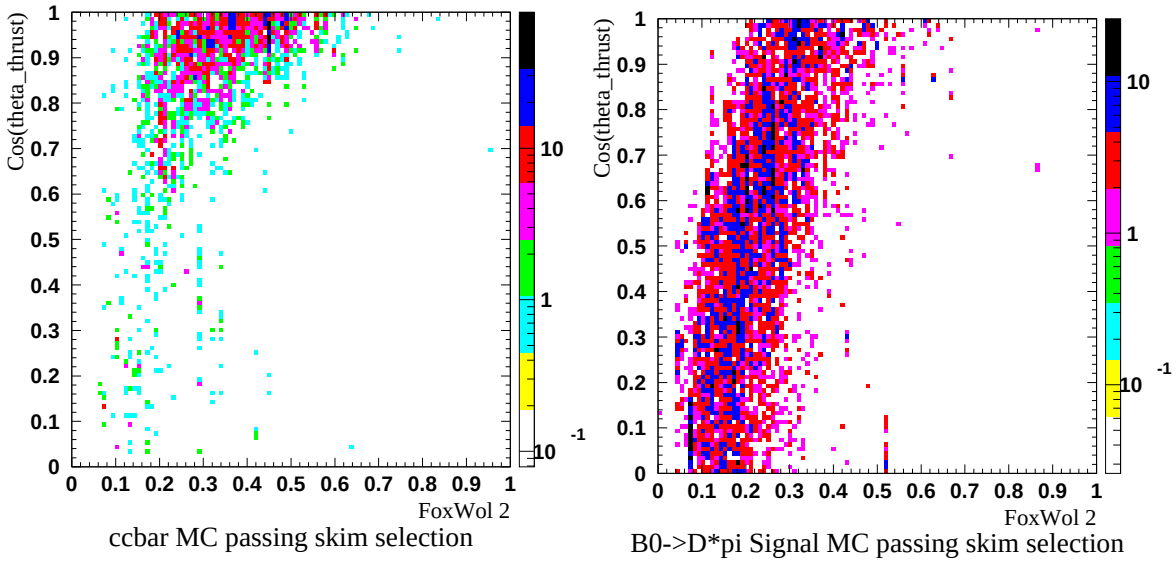

Figure 16: $\cos\theta_{th}$ vs. R_2 for Monte Carlo signal samples for generic $c\overline{c}$ and $\overline{B}^0 \to D^{*+}\pi^-$, $D^0 \to K^-\pi^+$. Although these variables are correlated, the thrust angle selection still has significant continuum background rejection power even after the R_2 selection is applied.

We further reduce backgrounds in some of the lower-purity modes by using a thrust-angle technique. The 'thrust angle', θ_{th}, is defined as the angle between the thrust axis of the particles which form the reconstructed B candidate and the thrust axis of the remaining tracks and unmatched clusters in the event, computed in the $\Upsilon(4S)$ frame. The two axes are

[4] A detailed optimization study is in progress.

almost completely uncorrelated in $B\overline{B}$ events, because the B mesons are almost at rest in the $\Upsilon(4S)$ rest frame, and the distribution in $|\cos\theta_{th}|$ given in Fig. 17 for the decay mode $\overline{B}^0 \to D^{*+}\pi^-$, $D^0 \to K^-\pi^+$. In continuum events, which are more jetlike, the two thrust axes tend to have small opening angles. Requiring $|\cos\theta_{th}| < 0.8$ typically removes about xx% of the continuum background while retaining 80% of the signal. The selection criteria $|\cos\theta_{th}|$ that depends on mode and is summarized in Table 17.

Mode	$\lvert\cos\theta_{th}\rvert$ cut
$B^0 \to D^{*-}\pi^+$	No cut
$B^0 \to D^{*-}\rho^+$	No cut
$B^0 \to D^{*-}a_1^+$	No cut
$B^0 \to D^-\pi^+$	< 0.9
$B^0 \to D^-\rho^+$	< 0.8
$B^0 \to D^-a_1^+$	< 0.7
$B^+ \to D^{*0}\pi^+$	< 0.9

Table 17: Thrust angle cuts applied in the each B decay channel under study.

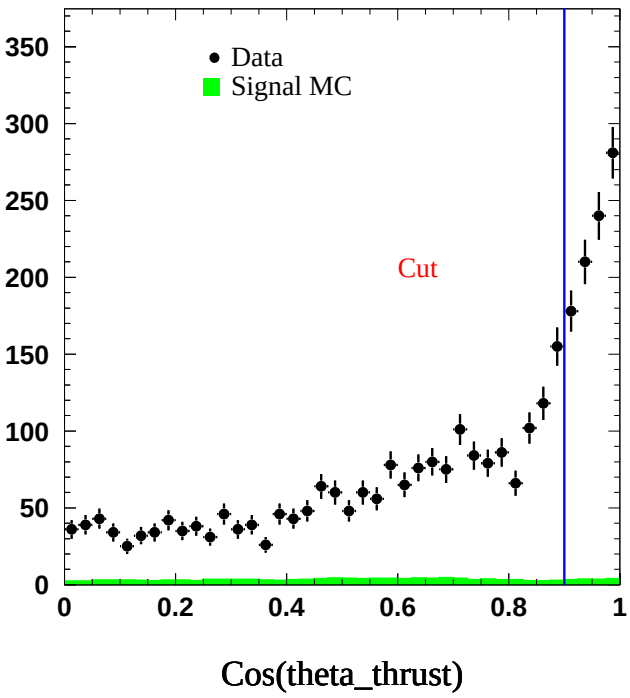

Figure 17: Distribution of the opening angle, θ_{th}, between thrust axes for the B candidate and the remaining tracks in the event for the mode $\overline{B}^0 \to D^{*+}\pi^-$, $D^0 \to K^-\pi^+$.

3.8 Background Fitting

The measurement of branching ratios, mixing and B lifetime require a good understanding of the shape of the background in the m_{ES} distribution. We expect the m_{ES} distribution from the ΔE sideband to provide important constraints about the background shape. However, this question is still under study both in data and Monte Carlo simulation. For the time being, we assume a background shape given by the ARGUS function, which parametrizes how phase space approaches zero as the candidate energy approaches E^*_{beam}:

$$f_{BG}(x) \;=\; Nx\sqrt{1-x^2}\exp(\kappa(1-x^2)) \tag{3}$$

where $x = m_{ES}/E^*_{beam}$, and the normalization and the shape are determined by the parameters N and κ. To determine the number of signal events from the m_{ES} distribution in the ΔE interval centered at zero, we make a fit using the ARGUS background function and a Gaussian signal with free mass, m_B, and width, $\sigma_{m_{ES}}$. For projections of the signal as a function of ΔE a fit to the ΔE distribution is made using a linear background function plus a single Gaussian distribution with free mean and width, $\sigma_{\Delta E}$.

4 B^0 Decay Studies

Here we provide tables of resolutions and yields for the B^0 decay modes reconstructed. Additional selection criteria for branching ratio measurements are described in section 6.

A sample plot showing the ΔE versus m_{ES} distribution for $\overline{B}^0 \to D^{*+}\pi^-$, $D^0 \to K^-\pi^+$ is given in Figure 18

For each individual decay chain, the distribution of m_{ES} for $|\Delta E\ | < 3\sigma_{\Delta E}$ and ΔE for $|m_{ES} - m^0_{ES}| < 3\sigma_{m_{ES}}$ is provided. The same plots are also shown summed over D^0 or D^+ modes. These are shown as Figures 19 through 34

The fit results for $\sigma_{m_{ES}}$ and $\sigma_{\Delta E}$ in Monte Carlo and data are summarized in Table 18. The fitted numbers of events and estimated efficiencies are shown in Table 19.

The distribution of the thepolar angle, θ_B, between the B candidate momentum and the boost direction in the $\Upsilon(4S)$ frame is shown in Figure 36 for the sum of all $\overline{B}^0 \to D^{*+}\pi^-$ and $\overline{B}^0 \to D^{*+}\rho^-$ channels. These show the expected $\sin^2\theta_B$ distribution for the signal, but are flat for candidates in the m_{ES} sideband.

A number of problems are evident in the data and are under investigation:

- Mean value of ΔE is shifted to negative values; this will be re-examined with the new database energy values in the Osaka dataset.
- Observed spread of signal in ΔE is greater than predicted; the prediction will be studied with micro-level degradation of p_T resolution to better match control samples;
- Observed widths for m_{ES} are larger than expected in several decay chains, particularly those in $\overline{B}^0 \to D^{*+}\rho^-$ channel. This is under investigation.
- There is also a discrepancy for $\overline{B}^0 \to D^{*+}\rho^-$ between the fitted number of events obtained from the m_{ES} distribution versus that extracted from the ΔE fit, with the latter always somewhat smaller. Further work on understanding the shape of the

backgrounds in the two distributions will be required, using the ΔE sidebands and generic Monte Carlo.

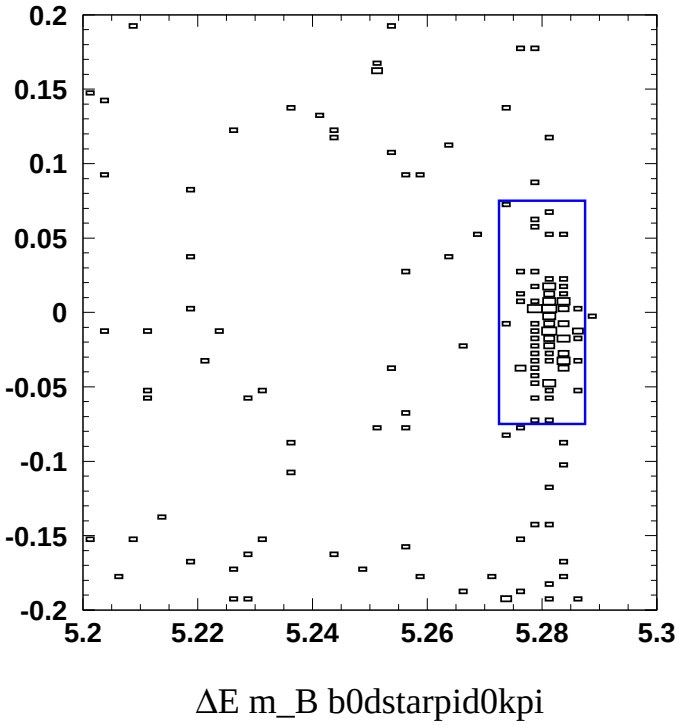

Figure 18: ΔE versus m_{ES} for the decay $\overline{B}^0 \to D^{*+}\pi^-$, $D^0 \to K^-\pi^+$.

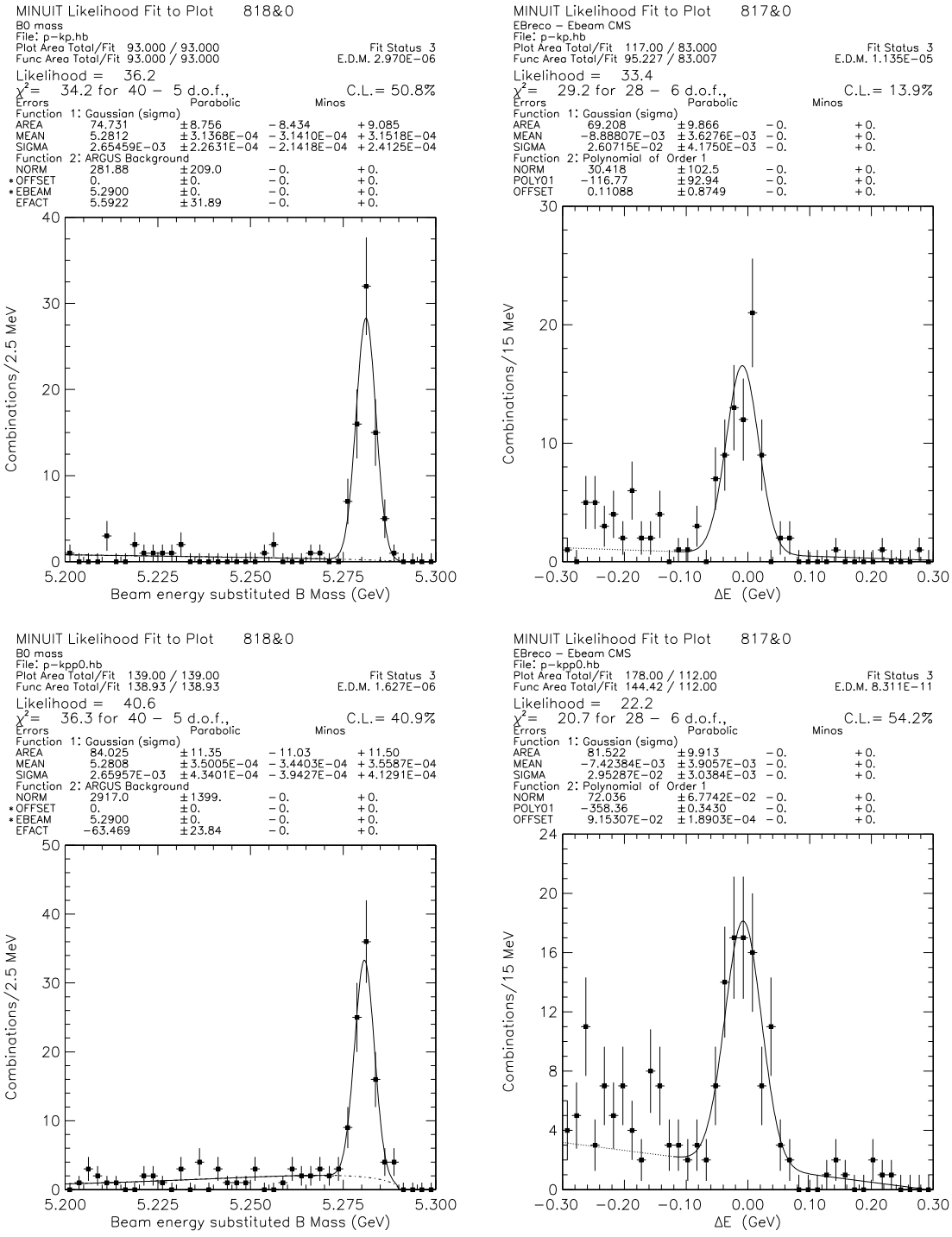

Figure 19: $\overline{B}^0 \to D^{*+}\pi^-$ for $D^0 \to K^-\pi^+$ (top) and $D^0 \to K^-\pi^+\pi^0$ (bottom). m_{ES} for $|\Delta E\ | < 2.5\sigma_{\Delta E}$ (left), ΔE for $|m_{ES} - m_B| < 2.5\sigma_{m_{ES}}$ (right).

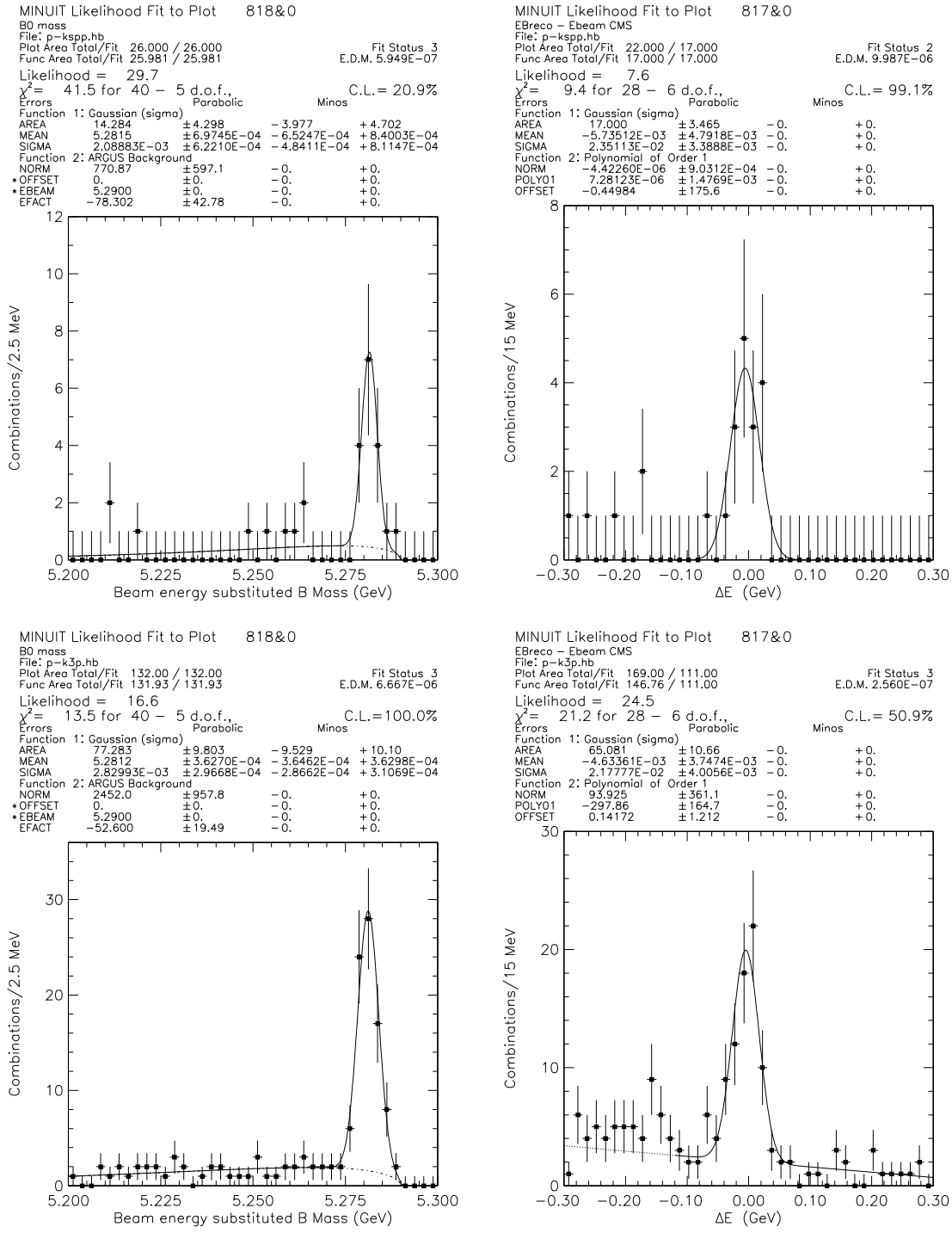

Figure 20: $\overline{B}^0 \to D^{*+}\pi^-$ for $D^0 \to K^0_S\pi^+\pi^-$ (top) and $D^0 \to K^-\pi^+\pi^-\pi^+$ (bottom). m_{ES} for $|\Delta E\ | < 2.5\sigma_{\Delta E}$ (left), ΔE for $|m_{ES} - m_B| < 2.5\sigma_{m_{ES}}$ (right).

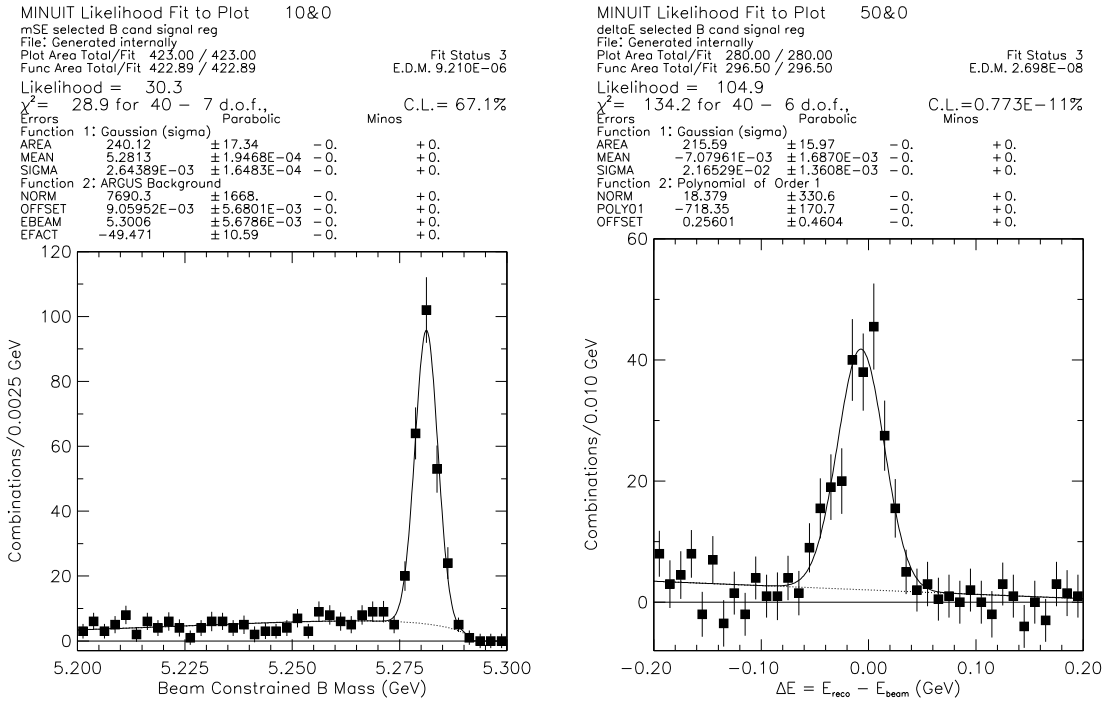

Figure 21: All D^0 modes for $\overline{B}^0 \to D^{*+}\pi^-$; m_{ES} for $|\Delta E\ | < 3\sigma_{\Delta E}$ (left), ΔE for $|m_{ES} - m_B| < 3\sigma_{m_{ES}}$ (right). The ΔE distribution has been obtained after sideband subtraction, defining the region for m_{ES} between 5.20 and 5.270 GeV/c^2 as sideband, and $m_{ES} > 5.275$ GeV/c^2 as signal. The relative normalization of the subtraction assumes a flat background across this full range of $m_{ES} > 5.2$ GeV/c^2.

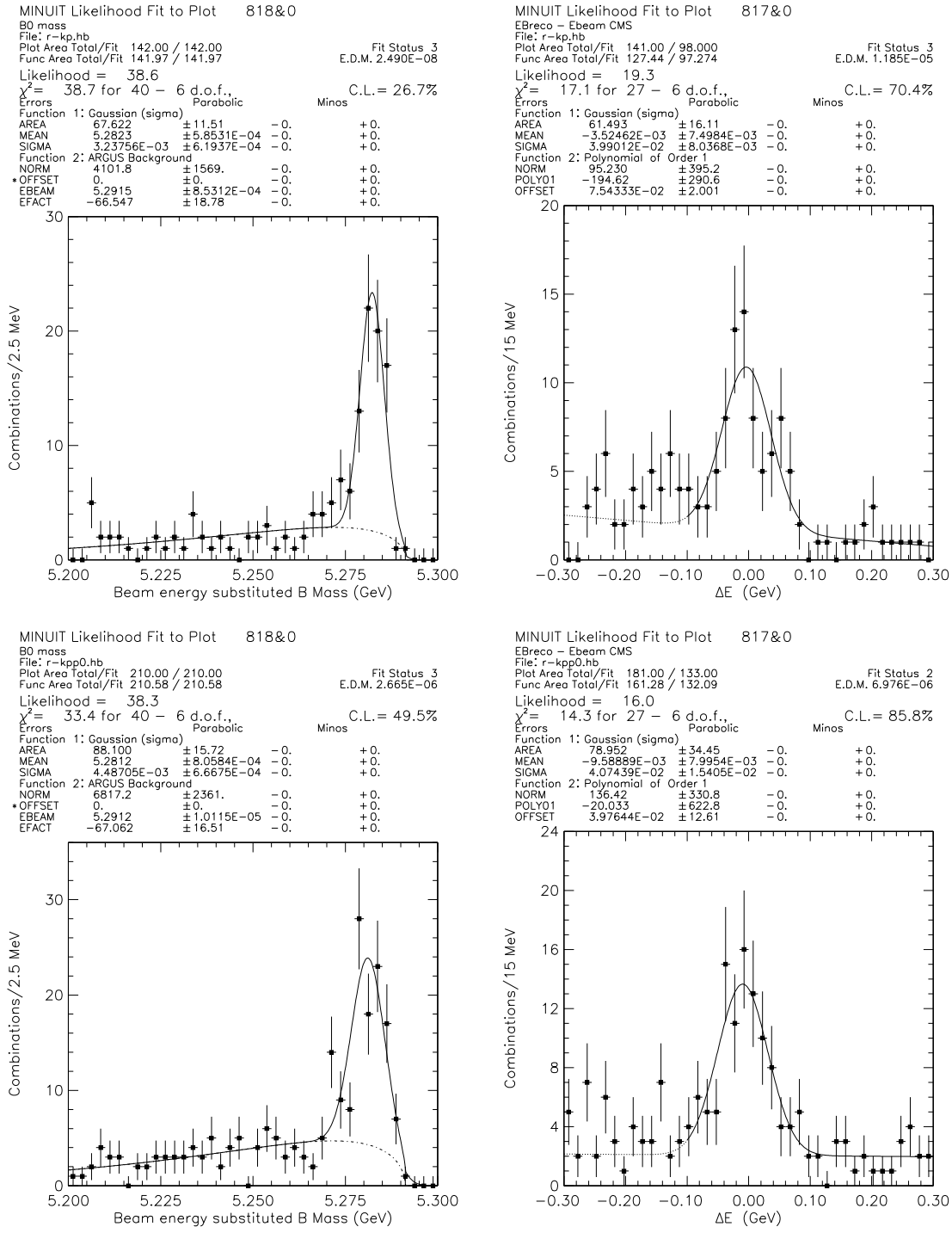

Figure 22: $\overline{B}^0 \to D^{*+}\rho^-$ for $D^0 \to K^-\pi^+$ (top) and $D^0 \to K^-\pi^+\pi^0$ (bottom). m_{ES} for $|\Delta E\ | < 2.5\sigma_{\Delta E}$ (left), ΔE for $|m_{ES} - m_B| < 2.5\sigma_{m_{ES}}$ (right).

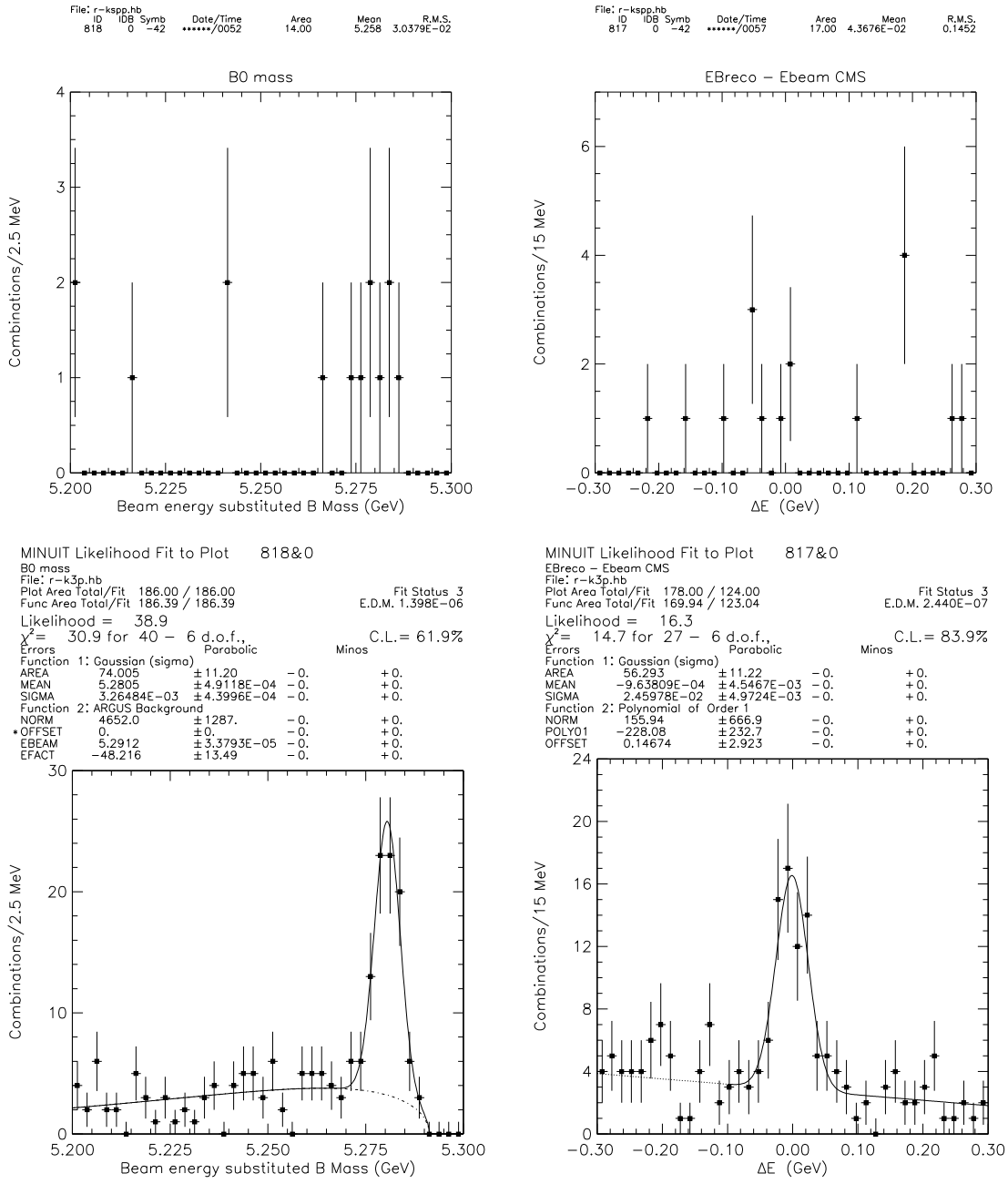

Figure 23: $\overline{B}^0 \to D^{*+}\rho^-$ for $D^0 \to K^0_S\pi^+\pi^-$ (top) and $D^0 \to K^-\pi^+\pi^-\pi^+$ (bottom). m_{ES} for $|\Delta E\ | < 2.5\sigma_{\Delta E}$ (left), ΔE for $|m_{ES} - m_B| < 2.5\sigma_{m_{ES}}$ (right).

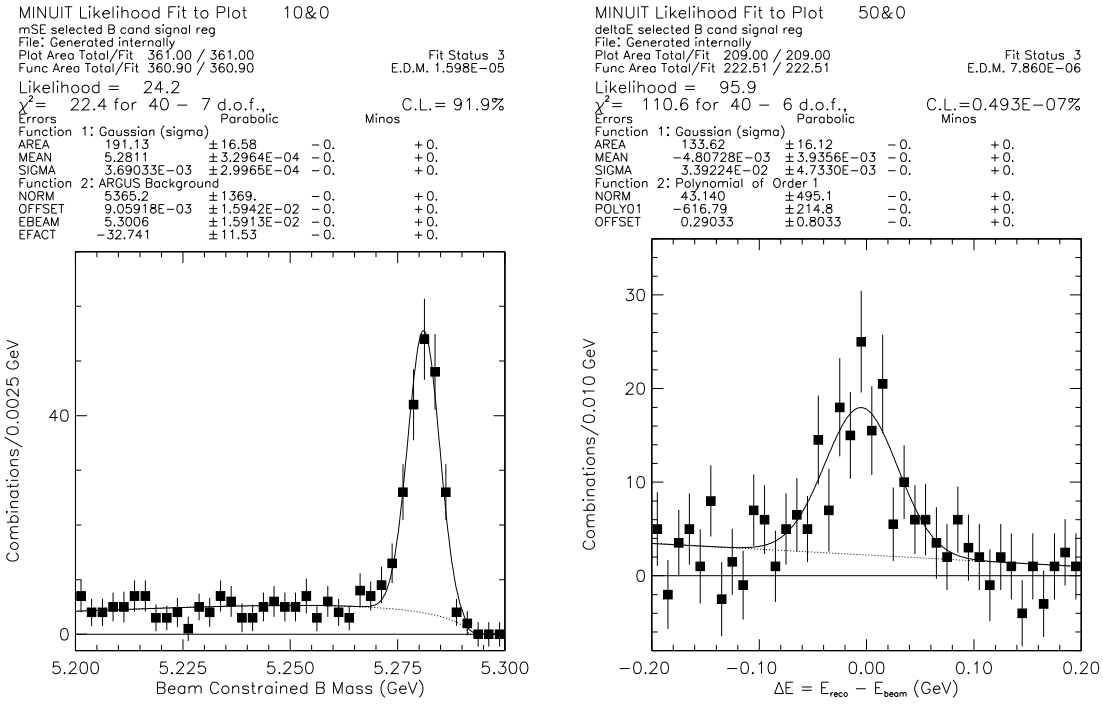

Figure 24: All D^0 modes for $\overline{B}^0 \to D^{*+}\rho^-$; m_{ES} for $|\Delta E\ | < 3\sigma_{\Delta E}$ (left), ΔE for $|m_{ES} - m^0_{ES}| < 3\sigma_{m_{ES}}$ (right). The ΔE distribution has been obtained after sideband subtraction, defining the region for m_{ES} between 5.20 and 5.270 GeV/c^2 as sideband, and $m_{ES} > 5.275$ GeV/c^2 as signal. The relative normalization of the subtraction assumes a flat background across this full range of $m_{ES} > 5.2$ GeV/c^2.

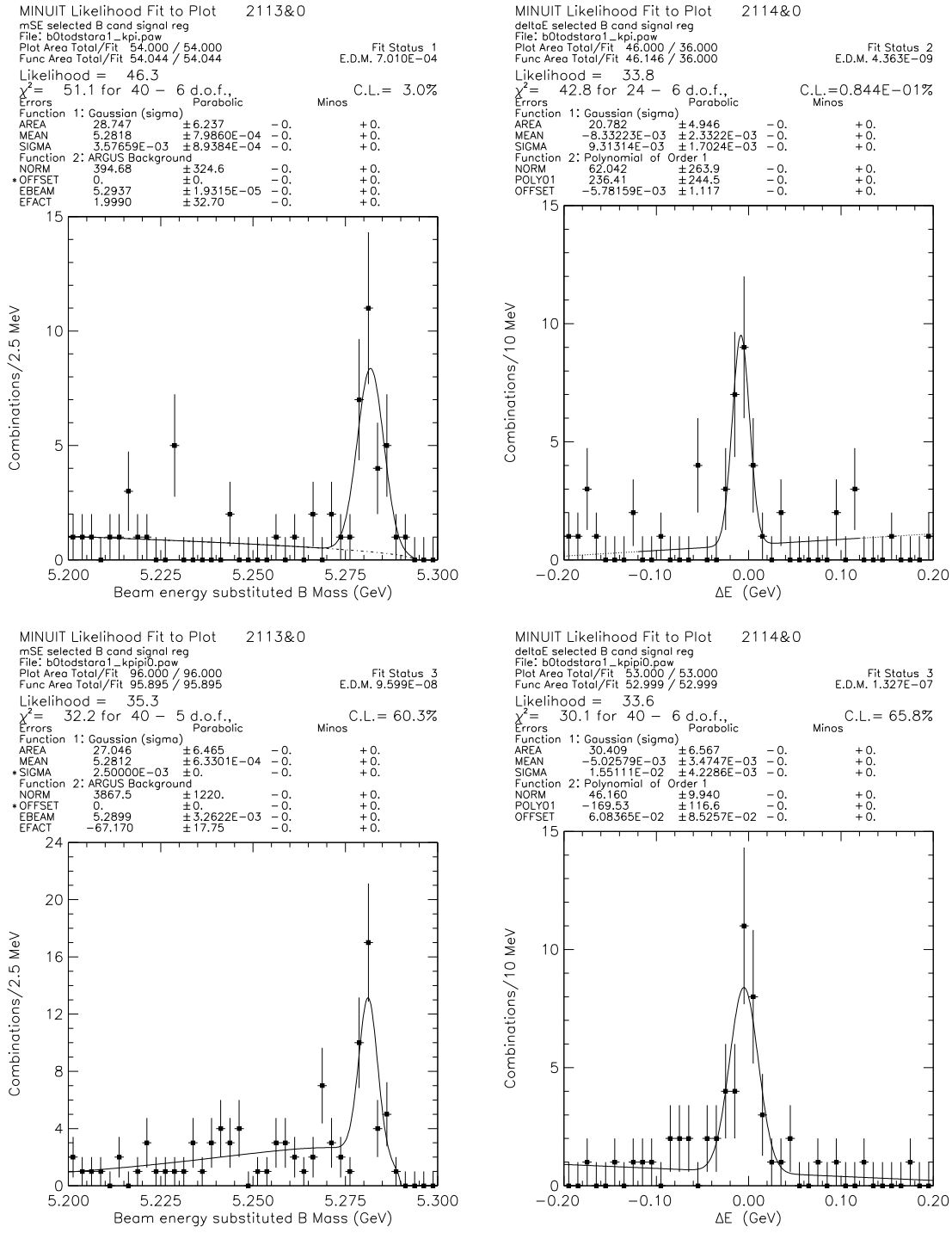

Figure 25: $\overline{B}^0 \to D^{*+}a_1^-$ for $D^0 \to K^-\pi^+$ (top) and $D^0 \to K^-\pi^+\pi^0$ (bottom). m_{ES} for $|\Delta E\ | < 3\sigma_{\Delta E}$ (left), ΔE for $|m_{ES} - m_{ES}^0| < 3\sigma_{m_{ES}}$ (right).

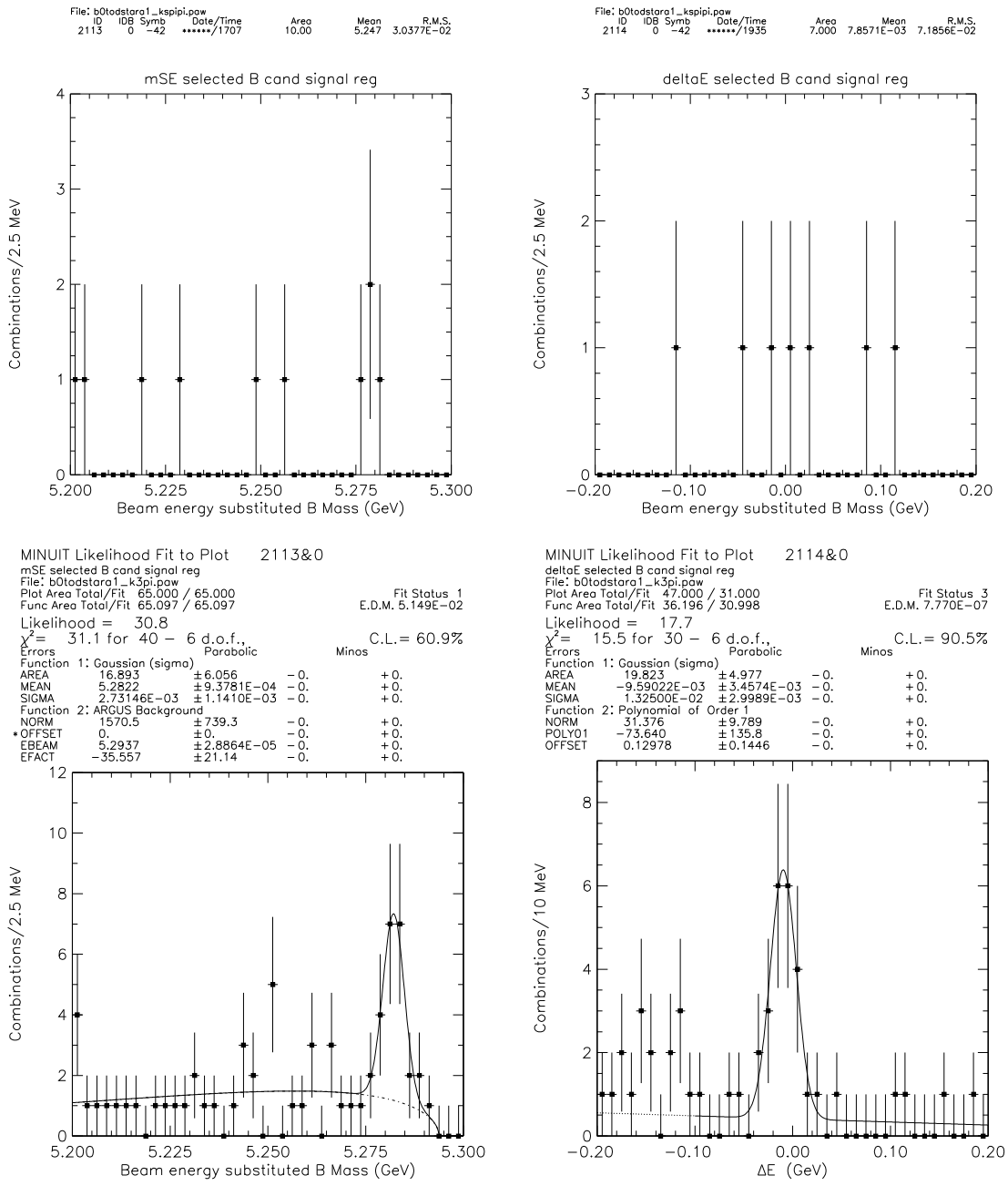

Figure 26: $\overline{B}^0 \to D^{*+}a_1^-$ for $D^0 \to K_S^0\pi^+\pi^-$ (top) and $D^0 \to K^-\pi^+\pi^-\pi^+$ (bottom). m_{ES} for $|\Delta E| < 3\sigma_{\Delta E}$ (left), ΔE for $|m_{ES} - m_{ES}^0| < 3\sigma_{m_{ES}}$ (right).

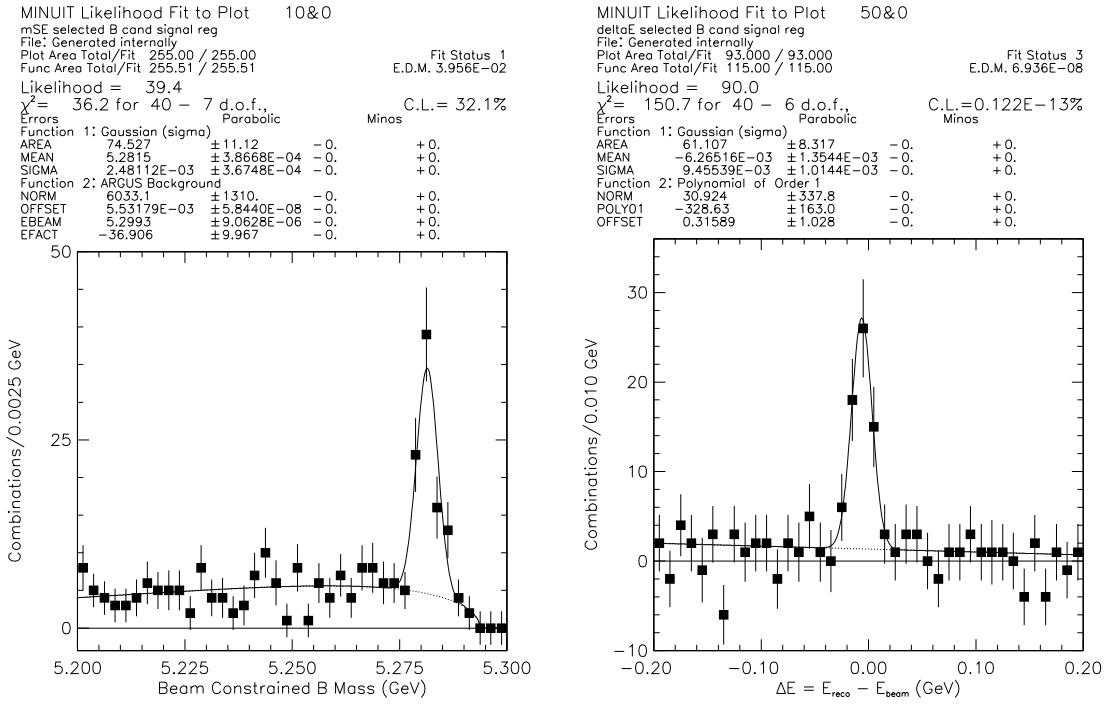

Figure 27: All D^0 modes for $\overline{B}^0 \to D^{*+}a_1^-$; m_{ES} for $|\Delta E\ | < 3\sigma_{\Delta E}$ (left), ΔE for $|m_{ES} - m^0_{ES}| < 3\sigma_{m_{ES}}$ (right). The ΔE distribution has been obtained after sideband subtraction, defining the region for m_{ES} between 5.20 and 5.270 GeV/c^2 as sideband, and $m_{ES} > 5.275$ GeV/c^2 as signal. The relative normalization of the subtraction assumes a flat background across this full range of $m_{ES} > 5.2$ GeV/c^2.

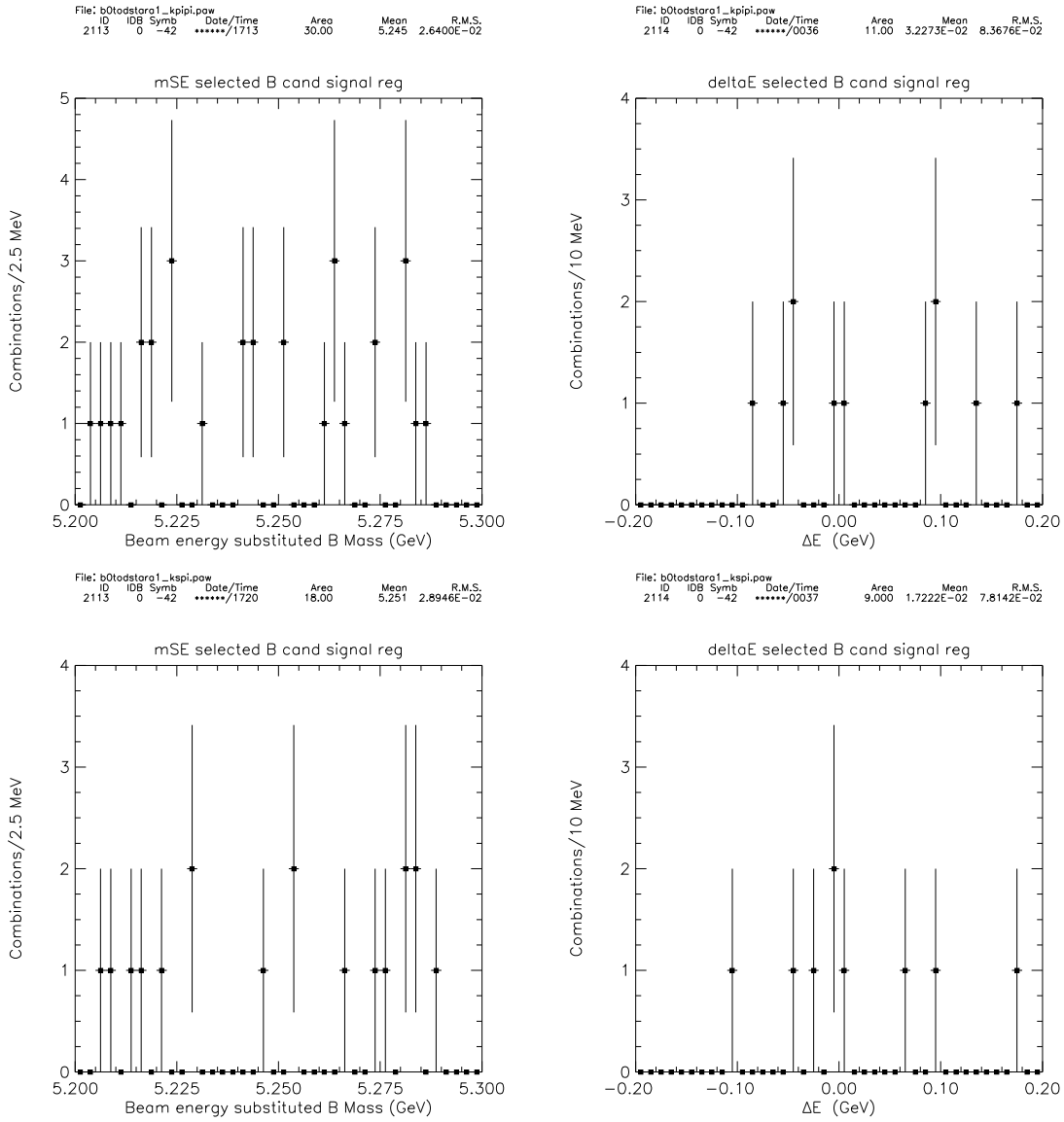

Figure 28: $\overline{B}^0 \to D^{*+}a_1^-$ for $D^+ \to K^-\pi^+\pi^+$ (top) and $D^+ \to K_S^0\pi^+$ (bottom). m_{ES} for $|\Delta E\ | < 3\sigma_{\Delta E}$ (left), ΔE for $|m_{ES} - m_{ES}^0| < 3\sigma_{m_{ES}}$ (right).

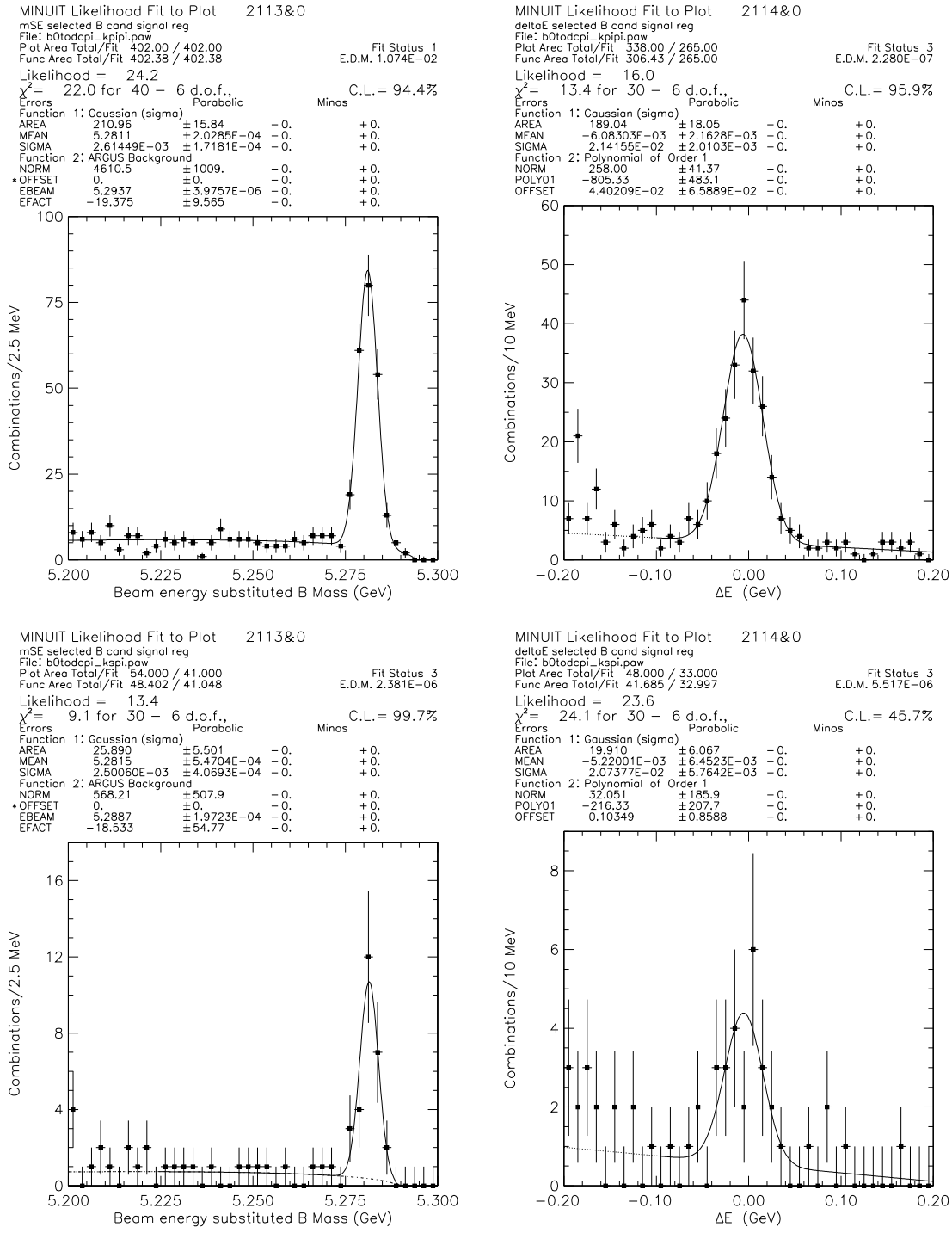

Figure 29: $\overline{B}^0 \to D^+\pi^-$ for $D^+ \to K^-\pi^+\pi^+$ (top) and $D^+ \to K^0_S\pi^+$ (bottom). m_{ES} for $|\Delta E\ | < 3\sigma_{\Delta E}$ (left), ΔE for $|m_{ES} - m^0_{ES}| < 3\sigma_{m_{ES}}$ (right).

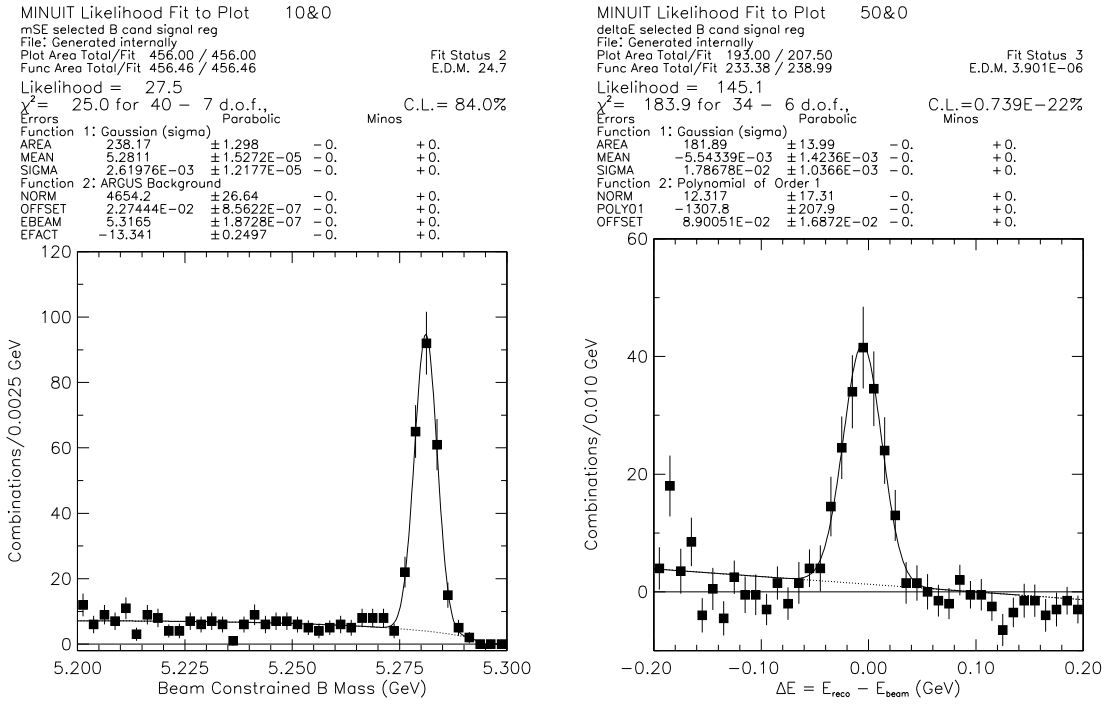

Figure 30: All D^+ modes for $\overline{B}^0 \to D^+\pi^-$; m_{ES} for $|\Delta E\ | < 3\sigma_{\Delta E}$ (left), ΔE for $|m_{ES} - m^0_{ES}| < 3\sigma_{m_{ES}}$ (right). The ΔE distribution has been obtained after sideband subtraction, defining the region for m_{ES} between 5.20 and 5.270 GeV/c^2 as sideband, and $m_{ES} > 5.275$ GeV/c^2 as signal. The relative normalization of the subtraction assumes a flat background across this full range of $m_{ES} > 5.2$ GeV/c^2.

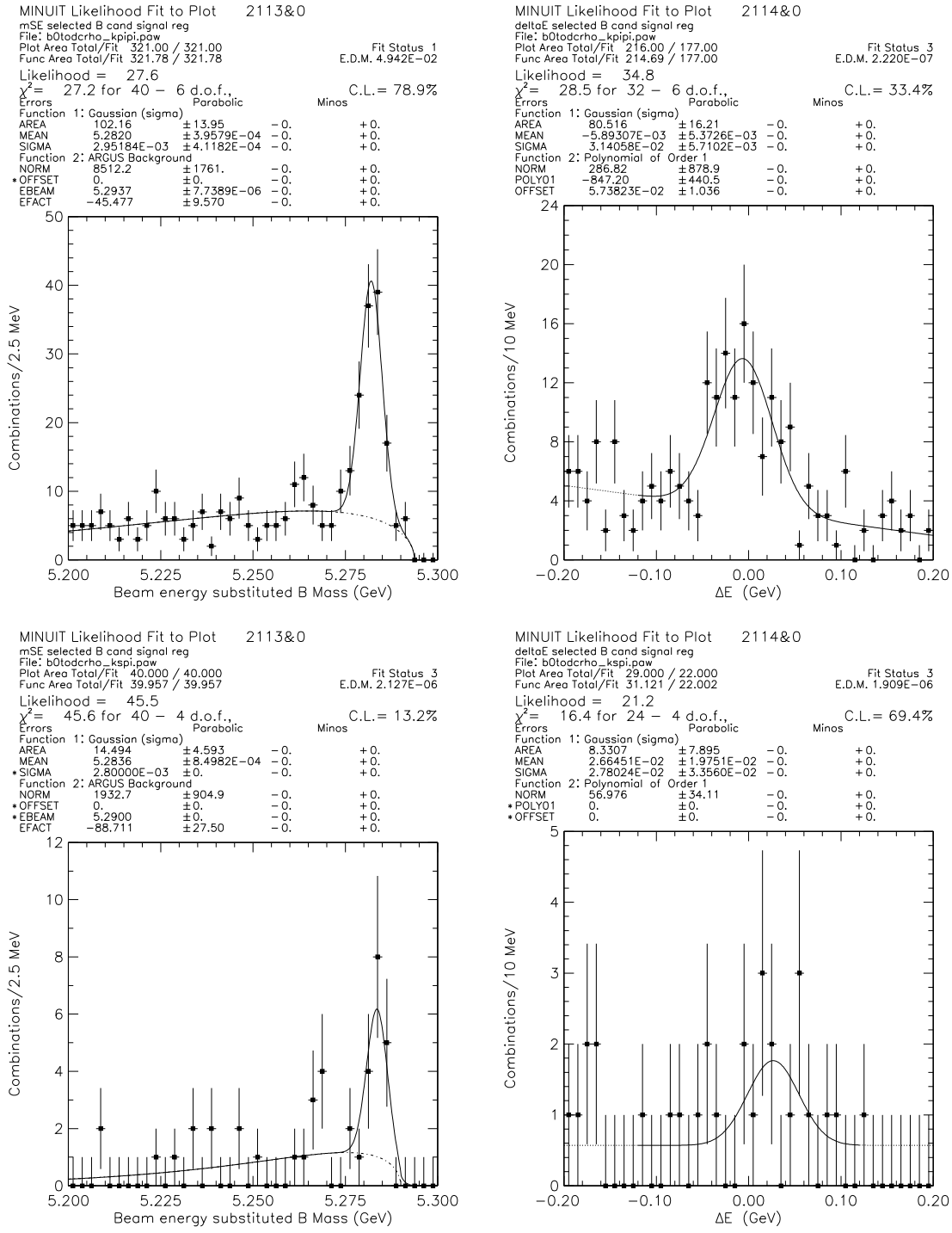

Figure 31: $\overline{B}^0 \to D^+\rho^-$ for $D^+ \to K^-\pi^+\pi^+$ (top) and $D^+ \to K^0_S\pi^+$ (bottom). m_{ES} for $|\Delta E\ | < 3\sigma_{\Delta E}$ (left), ΔE for $|m_{ES} - m^0_{ES}| < 3\sigma_{m_{ES}}$ (right).

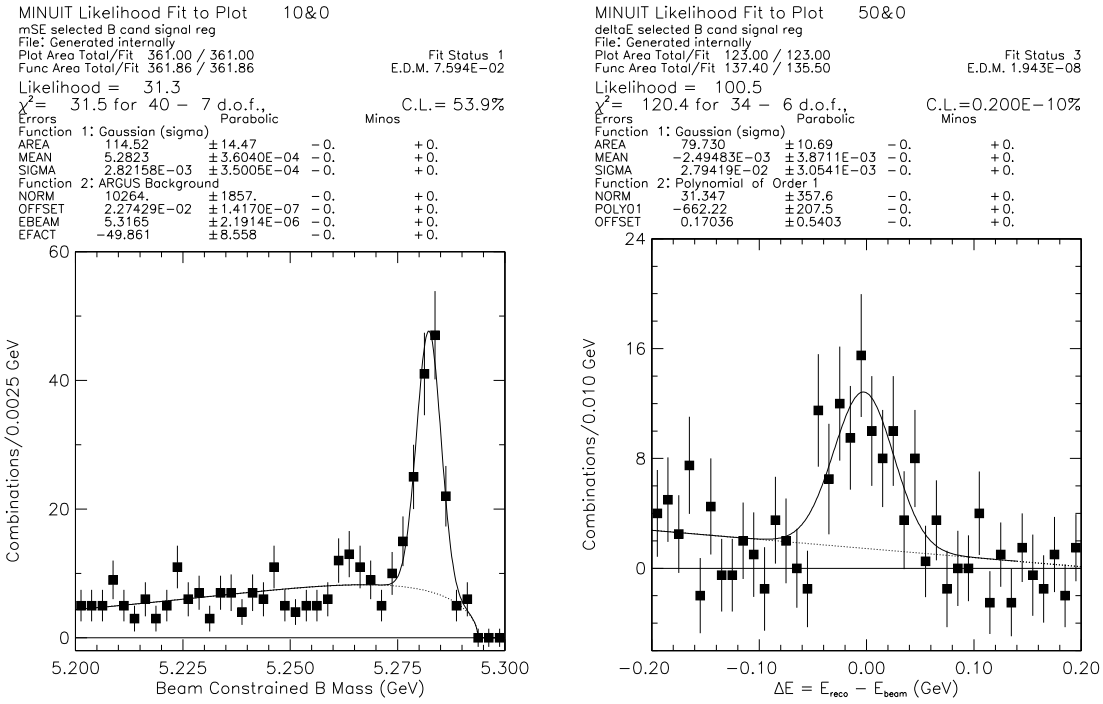

Figure 32: All D^+ modes for $\overline{B}^0 \to D^+\rho^-$; m_{ES} for $|\Delta E| < 3\sigma_{\Delta E}$ (left), ΔE for $|m_{ES} - m^0_{ES}| < 3\sigma_{m_{ES}}$ (right). The ΔE distribution has been obtained after sideband subtraction, defining the region for m_{ES} between 5.20 and 5.270 GeV/c^2 as sideband, and $m_{ES} > 5.275$ GeV/c^2 as signal. The relative normalization of the subtraction assumes a flat background across this full range of $m_{ES} > 5.2$ GeV/c^2.

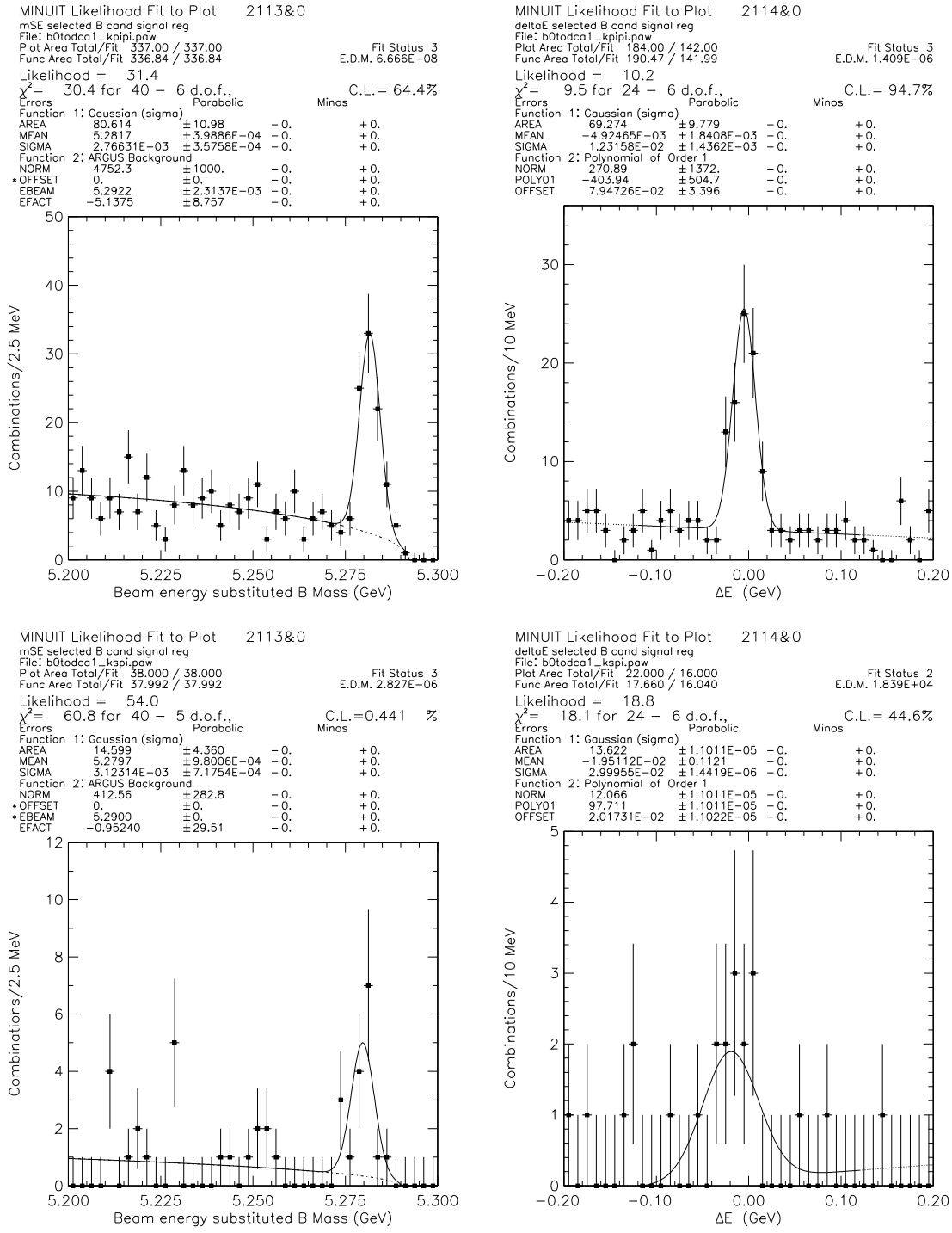

Figure 33: $\overline{B}^0 \to D^+ a_1^-$ for $D^+ \to K^-\pi^+\pi^+$ (top) and $D^+ \to K_S^0\pi^+$ (bottom). m_{ES} for $|\Delta E\ | < 3\sigma_{\Delta E}$ (left), ΔE for $|m_{ES} - m_{ES}^0| < 3\sigma_{m_{ES}}$ (right).

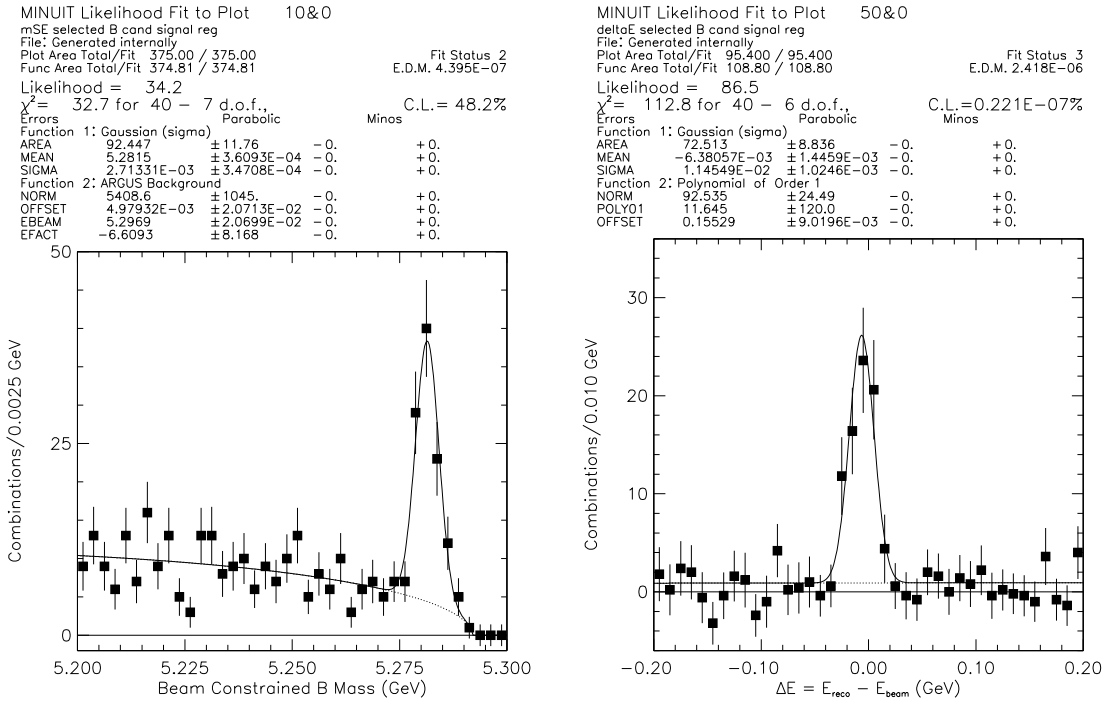

Figure 34: All D^+ modes for $\overline{B}^0 \to D^+ a_1^-$; m_{ES} for $|\Delta E| < 3\sigma_{\Delta E}$ (left), ΔE for $|m_{ES} - m^0_{ES}| < 3\sigma_{m_{ES}}$ (right). The ΔE distribution has been obtained after sideband subtraction, defining the region for m_{ES} between 5.20 and 5.270 GeV/c^2 as sideband, and $m_{ES} > 5.275$ GeV/c^2 as signal. The relative normalization of the subtraction assumes a flat background across this full range of $m_{ES} > 5.2$ GeV/c^2.

Table 18: Observed and predicted resolution for ΔE and m_{ES} for B^0 decay modes. In some cases, the fit results for individual decay chains suffer from inadequate statistics, particularly without full confidence in Monte Carlo predictions for signal widths.

B^0 mode	D mode	$\sigma_{\Delta E}$ Data (MeV)	ΔE offset (MeV)	$\sigma_{\Delta E}$ MC (MeV)	$\sigma_{m_{ES}}$ Data (MeV)	$\sigma_{m_{ES}}$ MC (MeV)
$D^{*-}\pi^+$	$K^-\pi^+$	26.1 ± 4.2	-8.9 ± 3.6	13.2 ± 0.2	2.7 ± 0.2	2.48 ± 0.03
	$K^-\pi^+\pi^0$	29.5 ± 3.0	-7.4 ± 3.9	16.5 ± 0.7	2.7 ± 0.4	2.8 ± 0.2
	$K^0_S\pi^+\pi^-$	23.5 ± 3.4	-5.7 ± 4.8	14.2 ± 0.6	2.1 ± 0.6	2.5 ± 0.1
	$K^-\pi^+\pi^+\pi^-$	21.8 ± 4.0	-4.6 ± 3.7	13.2 ± 0.6	2.8 ± 0.3	2.5 ± 0.1
$D^{*-}\rho^+$	$K^-\pi^+$	39.0 ± 8.0	-3.5 ± 7.5	24.5 ± 1.8	3.2 ± 0.6	3.1 ± 0.1
	$K^-\pi^+\pi^0$	40.7 ± 15.4	-9.6 ± 8.0	30.8 ± 4.2	4.6 ± 0.7	3.4 ± 0.3
	$K^0_S\pi^+\pi^-$	–	–	24.6 ± 2.3	–	2.5 ± 0.2
	$K^-\pi^+\pi^+\pi^-$	24.6 ± 5.0	-9.6 ± 4.5	25.0 ± 3.1	3.3 ± 0.4	2.7 ± 0.2
$D^{*-}a_1^+$	$K^-\pi^+$	9.3 ± 1.7	-8.3 ± 2.3	9.2 ± 1.1	3.5 ± 0.9	2.7 ± 0.2
	$K^-\pi^+\pi^0$	15.5 ± 4.2	-5.0 ± 3.5	12.5 ± 2.6	–	2.2 ± 0.2
	$K^0_S\pi^+\pi^-$	–	–	9.2 ± 1.2	–	2.4 ± 0.3
	$K^-\pi^+\pi^+\pi^-$	13.2 ± 3.0	-9.6 ± 3.4	8.0 ± 0.8	2.7 ± 1.1	2.1 ± 0.3
$D^-\pi^+$	$K^-\pi^+\pi^+$	21.4 ± 2.0	-6.1 ± 2.2	12.5 ± 0.4	2.6 ± 0.2	2.4 ± 0.1
	$K^0\pi^+$	20.7 ± 5.8	-5.2 ± 6.4	12.9 ± 0.4	2.5 ± 0.4	2.5 ± 0.1
$D^-\rho^+$	$K^-\pi^+\pi^+$	31.4 ± 5.7	-5.9 ± 5.4		3.0 ± 0.4	
	$K^0\pi^+$	–	–	–		
$D^-a_1^+$	$K^-\pi^+\pi^+$	–				
	$K^0\pi^+$	–				

Table 19: Observed and expected yields for B^0 decay modes. In some cases, the fit results for individual decay chains suffer from inadequate statistics, particularly without full confidence in Monte Carlo predictions for signal widths.

B^0 mode	D mode	Observed Yield	$\epsilon(\%)$	Expected Yield
$D^{*-}\pi^+$	$K^-\pi^+$	74.7 ± 8.8	32.6 ± 0.6	
	$K^-\pi^+\pi^0$	84.0 ± 11.3	10.2 ± 0.7	
	$K^0_S\pi^+\pi^-$	14.3 ± 4.3	17.2 ± 0.9	
	$K^-\pi^+\pi^+\pi^-$	77.3 ± 9.8	16.7 ± 0.9	
$D^{*-}\rho^+$	$K^-\pi^+$	67.6 ± 11.5	14.6 ± 0.9	
	$K^-\pi^+\pi^0$	88.1 ± 15.7	3.5 ± 0.4	
	$K^0_S\pi^+\pi^-$	–	6.4 ± 0.6	
	$K^-\pi^+\pi^+\pi^-$	74.0 ± 11.2	7.2 ± 0.6	
$D^{*-}a_1^+$	$K^-\pi^+$	28.7 ± 6.2	11.8 ± 1.0	
	$K^-\pi^+\pi^0$	27.0 ± 6.5	3.7 ± 0.6	
	$K^0_S\pi^+\pi^-$	–	4.5 ± 0.6	
	$K^-\pi^+\pi^+\pi^-$	16.9 ± 6.0	4.9 ± 0.8	
$D^-\pi^+$	$K^-\pi^+\pi^+$	211.0 ± 15.9	33.2 ± 1.3	
	$K^0\pi^+$	25.9 ± 5.5	39.0 ± 0.2	
$D^-\rho^+$	$K^-\pi^+\pi^+$	102.2 ± 13.9	$\pm$	
	$K^0\pi^+$	14.5 ± 4.5	$\pm$	
$D^-a_1^+$	$K^-\pi^+\pi^+$	$\pm$	$\pm$	
	$K^0\pi^+$	$\pm$	$\pm$	
Total				

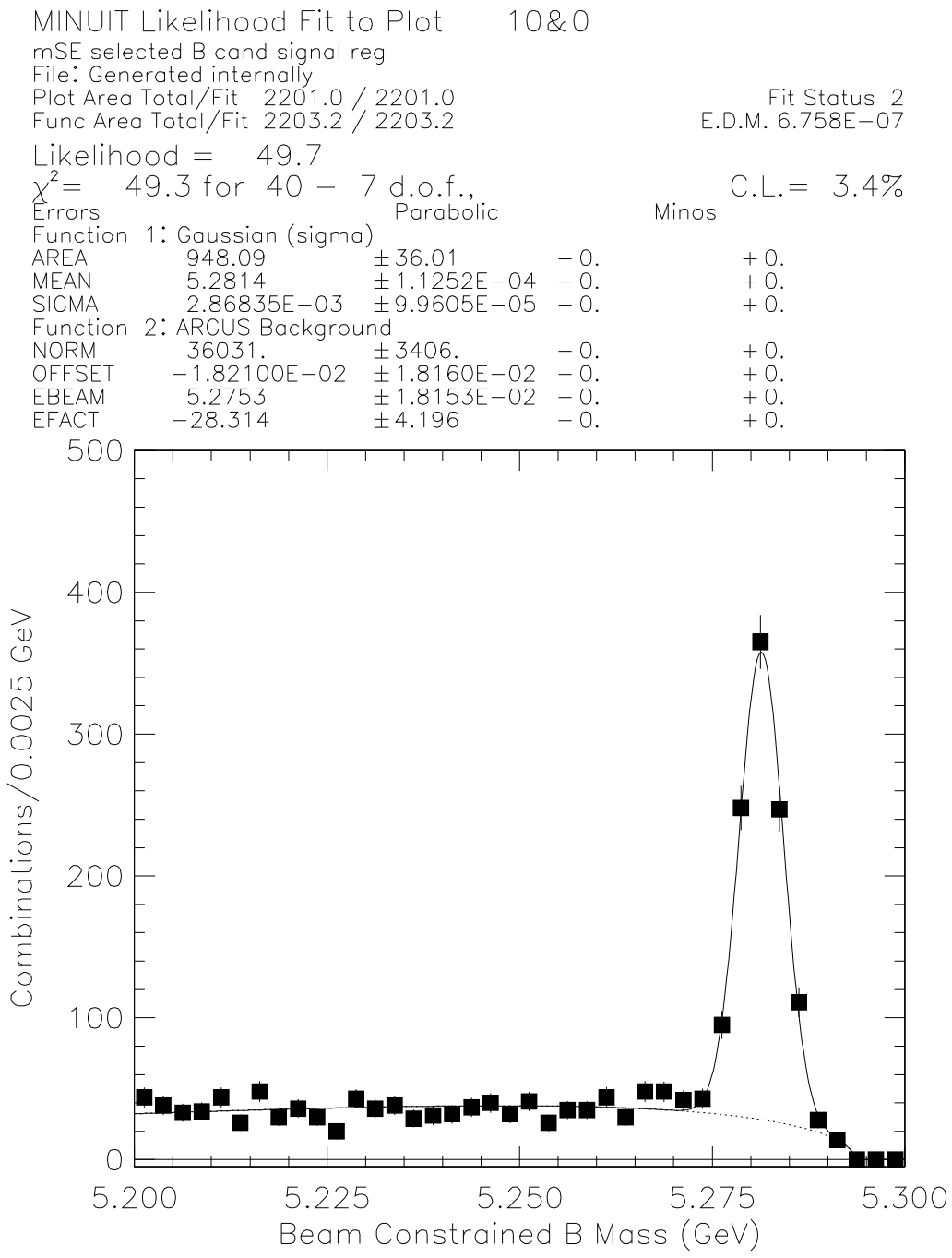

Figure 35: Combined distribution for m_{ES} from all hadronic B^0 modes.

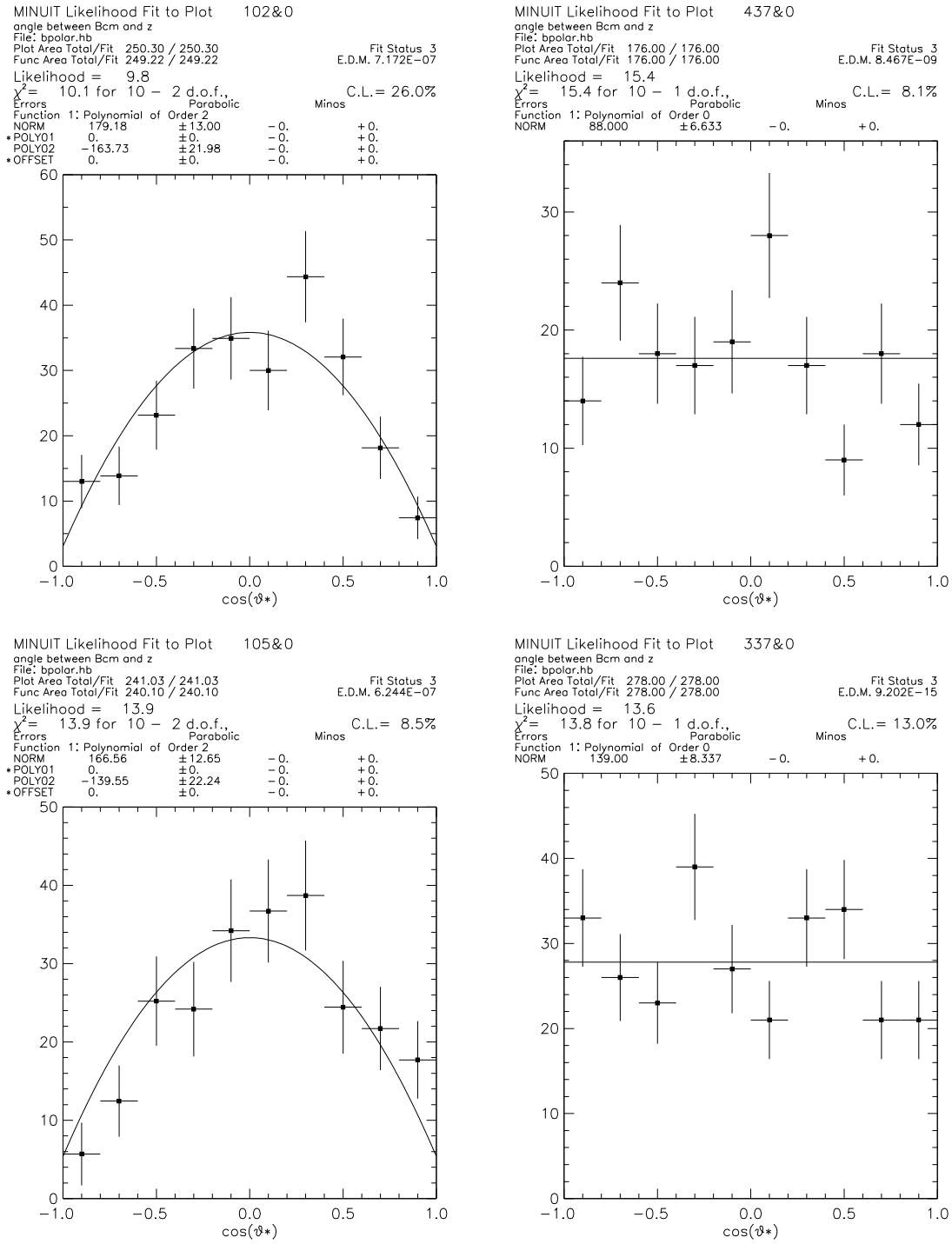

Figure 36: Distribution of the polar angle of the B candidates in the $\Upsilon(4S)$ frame for $\overline{B}^0 \to D^{*+}\pi^-$ (top) and $\overline{B}^0 \to D^{*+}\rho^-$ (bottom) using all D^0 modes, in the signal region after sideband subtraction (left) and in the sideband (right).

5 B^- Decays

Here we provide tables of resolutions and yields for the B^0 decay modes reconstructed. Additional selection criteria for branching ratio measurements are described in section 6.

For each individual decay chain, the distribution of m_{ES} for $|\Delta E| < 3\sigma_{\Delta E}$ and ΔE for $|m_{ES} - m_{ES}^0| < 3\sigma_{m_{ES}}$ is provided. The same plots are also shown summed over D^0 or D^+ modes. These are shown as Figures 37 through 34

The fit results for $\sigma_{m_{ES}}$ and $\sigma_{\Delta E}$ in Monte Carlo and data are summarized in Table 18. The fitted numbers of events and estimated efficiencies are shown in Table 19.

A number of problems are evident in the data and are under investigation:

- Mean value of ΔE is shifted to negative values; this will be re-examined with the new database energy values in the Osaka dataset;
- Observed spread of signal in ΔE is greater than predicted; the prediction will be studied with micro-level degradation of p_T resolution to better match control samples;
- Observed widths for m_{ES} are larger than expected in several decay chains, particularly those in $\overline{B}^0 \to D^{*+}\rho^-$ channel. This is under investigation.
- There is a discrepancy between the fitted number of events obtained from the m_{ES} distribution versus that extracted from the ΔE fit, with the latter always somewhat smaller. Further work on understanding the shape of the backgrounds in the two distributions will be required.

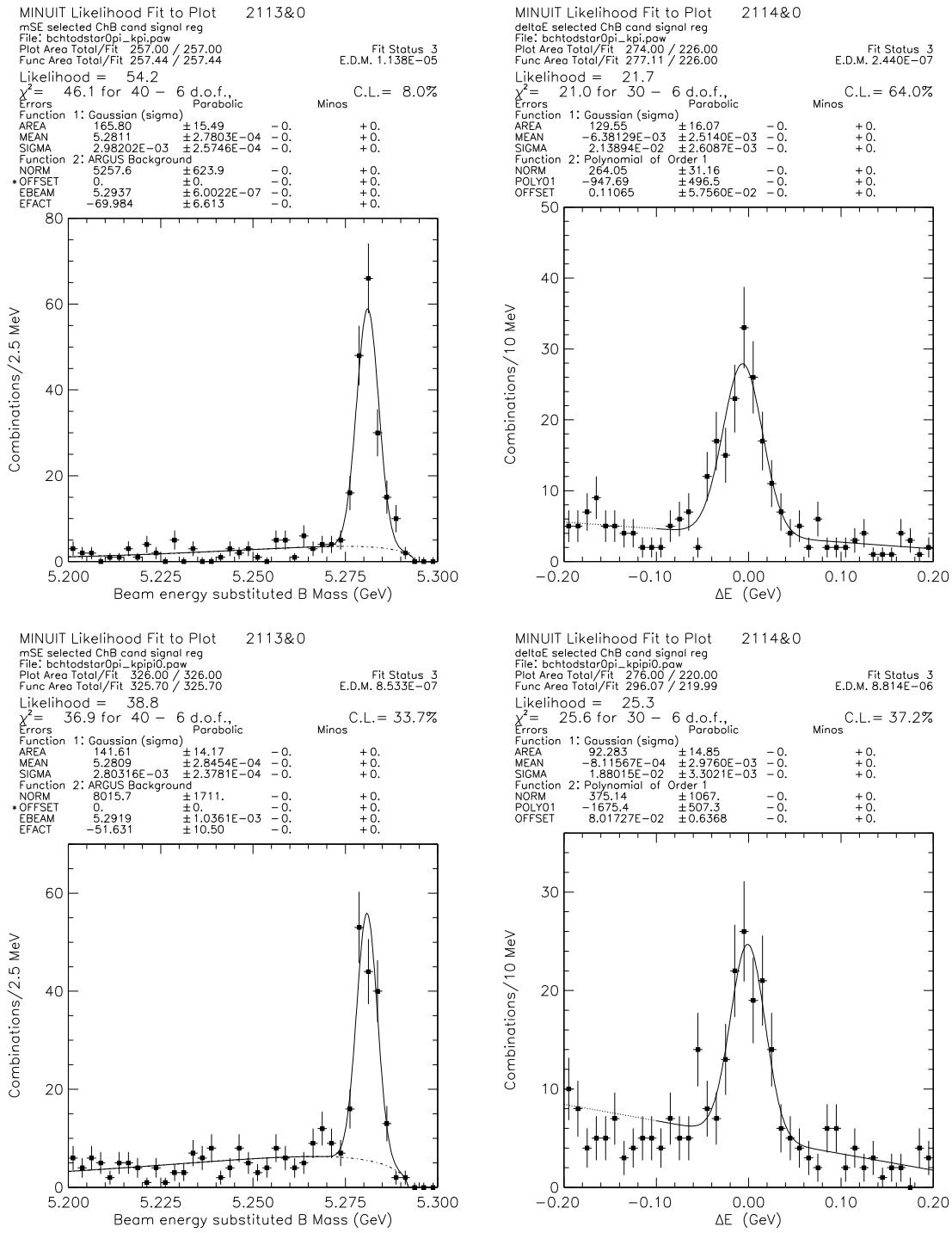

Figure 37: $B^- \to D^{*0}\pi$ for $D^0 \to K^-\pi^+$ (top) and $D^0 \to K^-\pi^+\pi^0$ (bottom). m_{ES} for $|\Delta E| < 3\sigma_{\Delta E}$ (left), ΔE for $|m_{ES} - m_{ES}^0| < 3\sigma_{m_{ES}}$ (right).

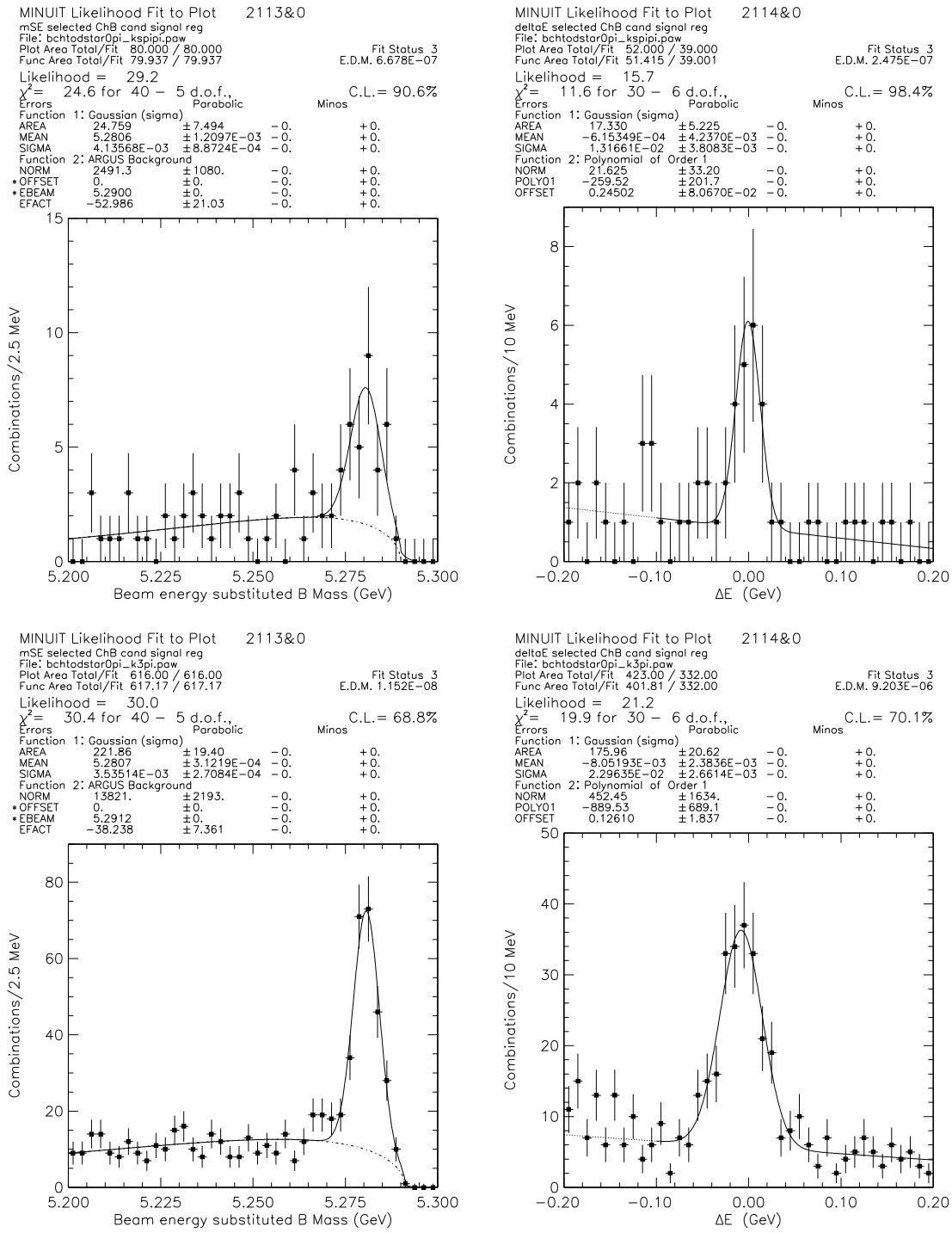

Figure 38: $B^- \to D^{*0}\pi$ for $D^0 \to K^0_S\pi^+\pi^-$ (top) and $D^0 \to K^-\pi^+\pi^-\pi^+$ (bottom). m_{ES} for $|\Delta E\ | < 3\sigma_{\Delta E}$ (left), ΔE for $|m_{ES} - m^0_{ES}| < 3\sigma_{m_{ES}}$ (right).

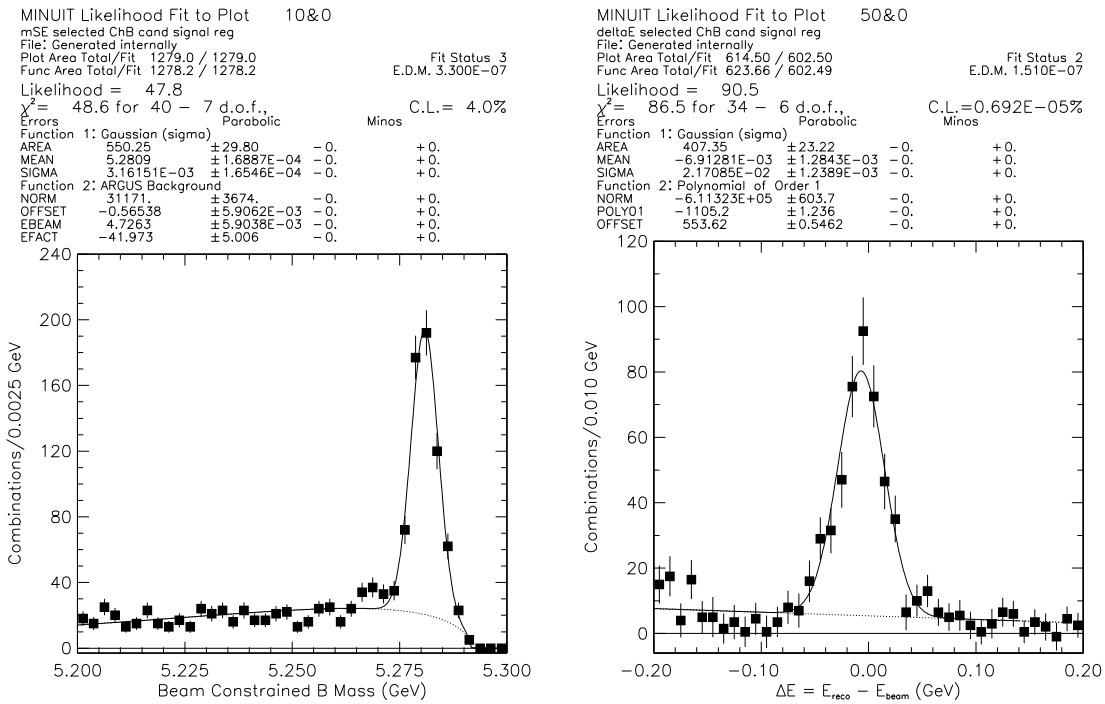

Figure 39: All D^0 modes for $B^- \to D^{*0}\pi^-$; m_{ES} for $|\Delta E\ | < 3\sigma_{\Delta E}$ (left), ΔE for $|m_{ES} - m^0_{ES}| < 3\sigma_{m_{ES}}$ (right). The ΔE distribution has been obtained after sideband subtraction, defining the region for m_{ES} between 5.20 and 5.270 GeV/c^2 as sideband, and $m_{ES} > 5.275$ GeV/c^2 as signal.

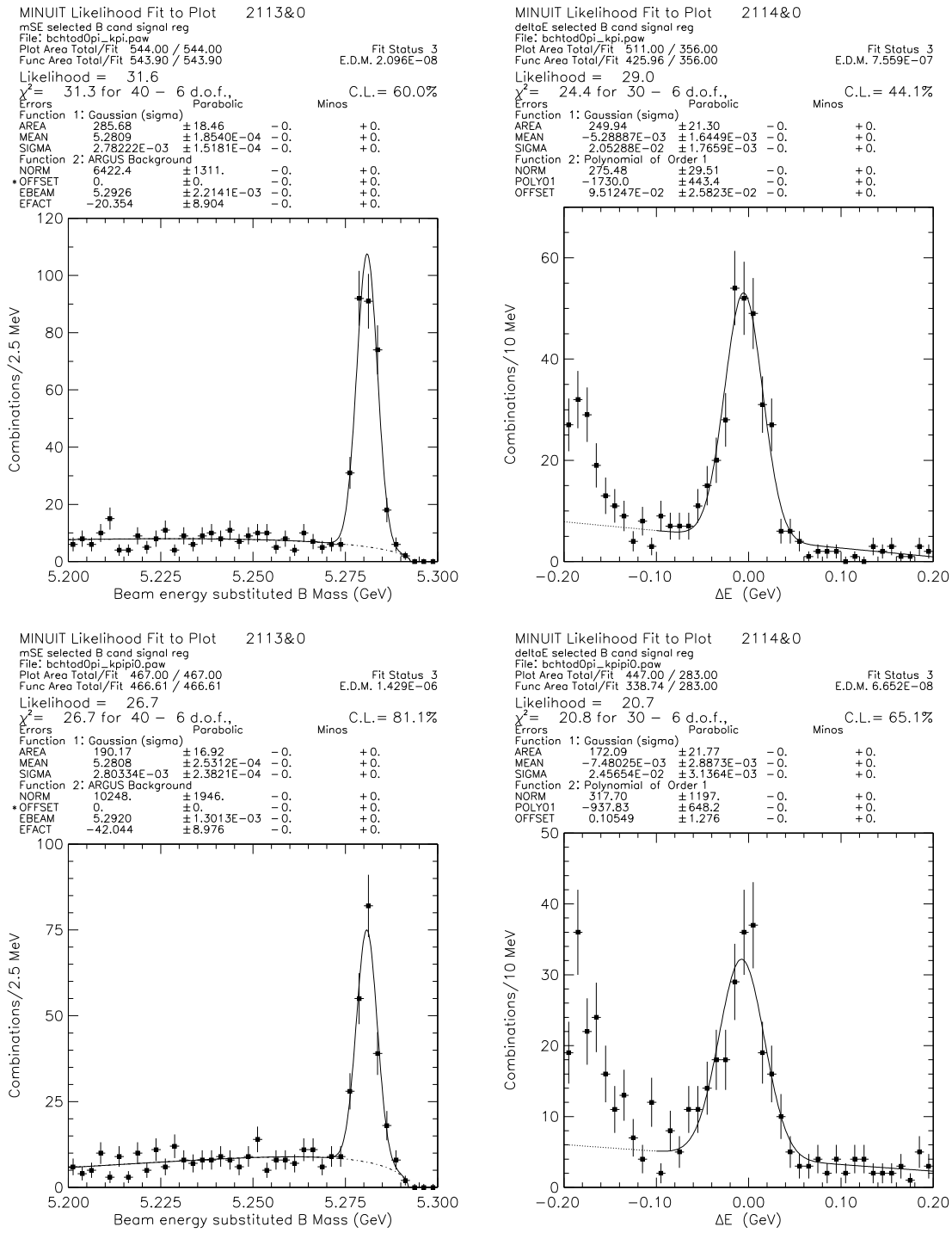

Figure 40: $B^- \to D^0\pi$ for $D^0 \to K^-\pi^+$ (top) and $D^0 \to K^-\pi^+\pi^0$ (bottom). m_{ES} for $|\Delta E| < 3\sigma_{\Delta E}$ (left), ΔE for $|m_{ES} - m_{ES}^0| < 3\sigma_{m_{ES}}$ (right).

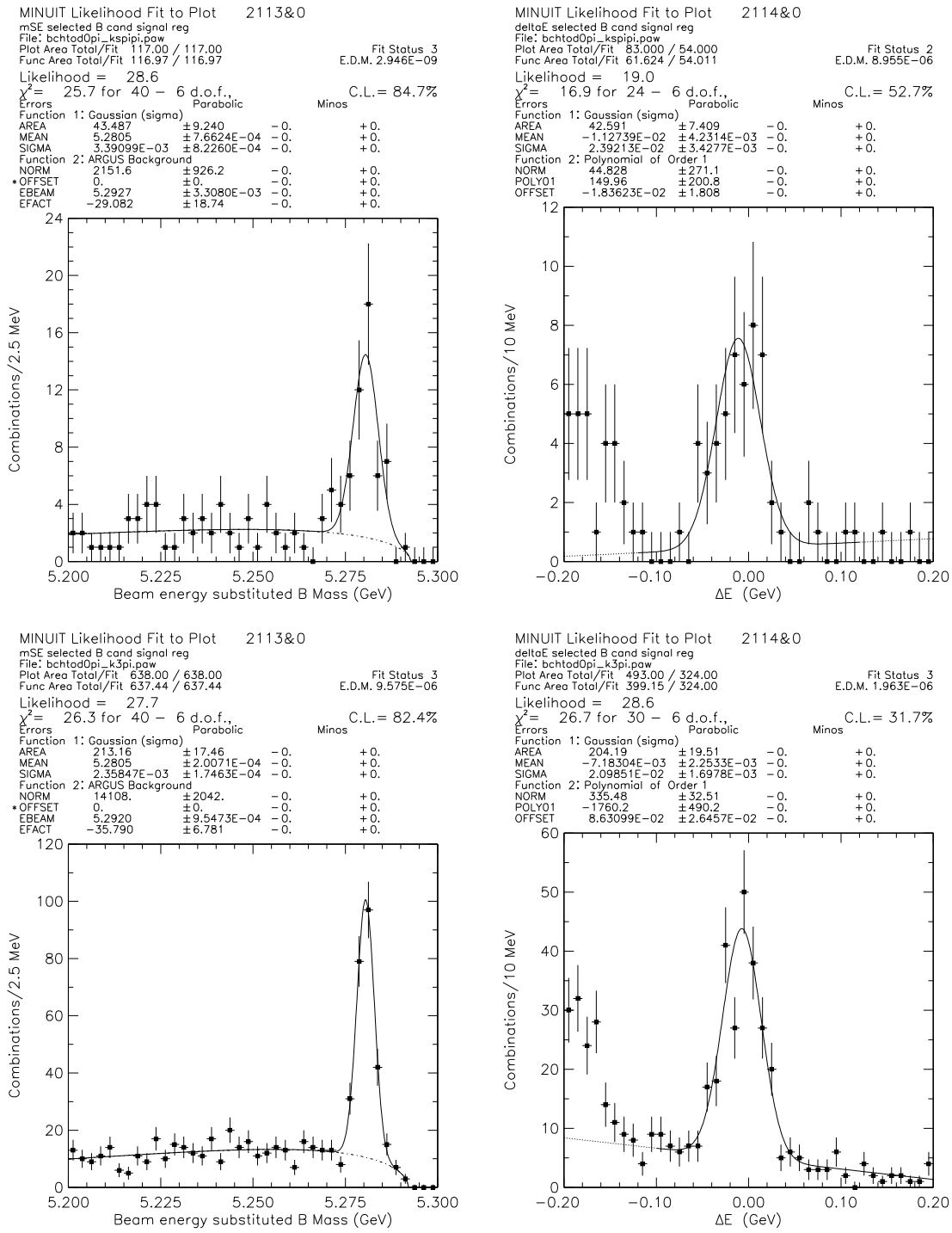

Figure 41: $B^- \to D^0\pi$ for $D^0 \to K^0_S\pi^+\pi^-$ (top) and $D^0 \to K^-\pi^+\pi^-\pi^+$ (bottom). m_{ES} for $|\Delta E\ | < 3\sigma_{\Delta E}$ (left), ΔE for $|m_{ES} - m^0_{ES}| < 3\sigma_{m_{ES}}$ (right).

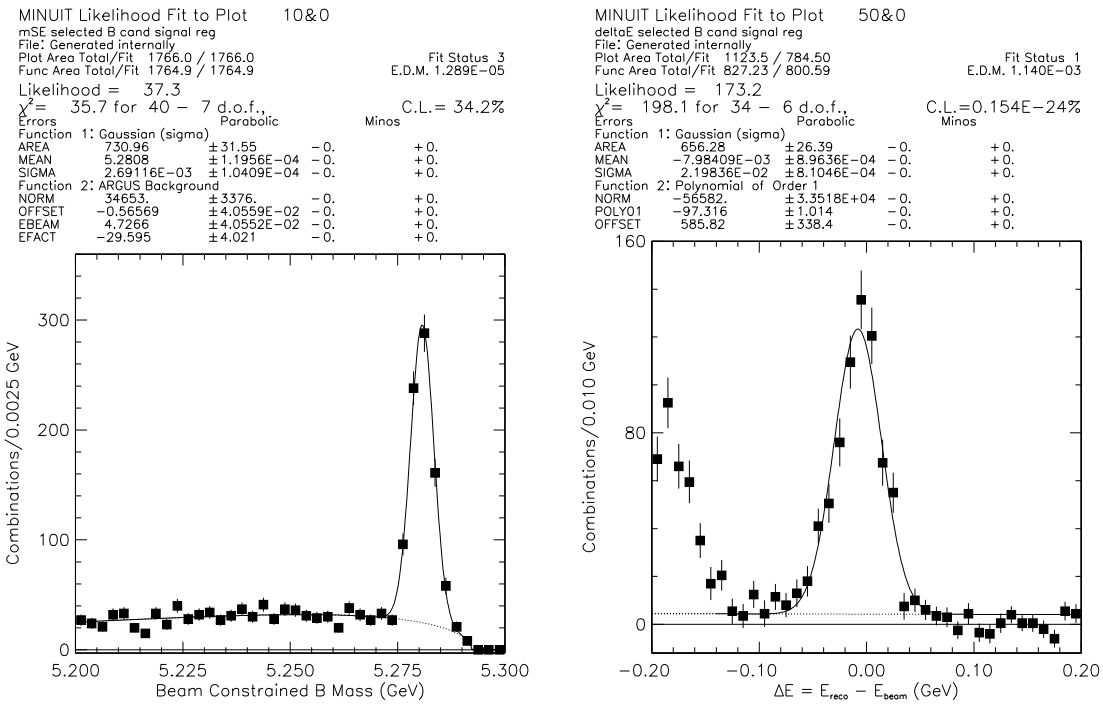

Figure 42: All D^0 modes for $B^- \to D^0\pi^-$; m_{ES} for $|\Delta E\ | < 3\sigma_{\Delta E}$ (left), ΔE for $|m_{ES} - m^0_{ES}| < 3\sigma_{m_{ES}}$ (right). The ΔE distribution has been obtained after sideband subtraction, defining the region for m_{ES} between 5.20 and 5.270 GeV/c^2 as sideband, and $m_{ES} > 5.275$ GeV/c^2 as signal.

Table 20: Observed and predicted resolution for ΔE and m_{ES} for B^- decay modes. In some cases, the fit results for individual decay chains suffer from inadequate statistics, particularly without full confidence in Monte Carlo predictions for signal widths.

B mode	D mode	$\sigma_{\Delta E}$ data	ΔE offset	$\sigma_{\Delta E}$ mc	$\sigma_{m_{ES}}$ data	$\sigma_{m_{ES}}$ mc
$D^{*0}\pi^+$	$K^-\pi^+$	21.4 ± 2.6	-6.4 ± 2.5	14.7 ± 0.5	3.0 ± 0.3	2.3 ± 0.1
	$K^-\pi^+\pi^0$	18.8 ± 3.3	-0.8 ± 3.0	19.6 ± 1.9	2.8 ± 0.2	2.3 ± 0.2
	$K^0_S\pi^+\pi^-$	13.2 ± 3.8	-0.6 ± 4.2	17.5 ± 1.3	4.1 ± 0.9	2.3 ± 0.2
	$K^-\pi^+\pi^+\pi^-$	23.0 ± 2.6	-8.0 ± 2.4	13.7 ± 0.1	3.5 ± 0.1	2.2 ± 0.1
$D^0\pi^+$	$K^-\pi^+$	20.5 ± 1.8	-5.3 ± 1.6	13.6 ± 0.4	2.8 ± 0.2	2.4 ± 0.1
	$K^-\pi^+\pi^0$	24.5 ± 3.1	-7.3 ± 2.9	14.8 ± 1.0	2.8 ± 0.2	2.5 ± 0.2
	$K^0_S\pi^+\pi^-$	23.9 ± 3.4	-11.3 ± 4.2	12.1 ± 0.4	3.4 ± 0.8	2.4 ± 0.2
	$K^-\pi^+\pi^+\pi^-$	21.0 ± 1.7	-7.2 ± 2.2	13.1 ± 0.5	2.4 ± 0.2	2.4 ± 0.1

Table 21: Observed and expected yields for B^- decay modes.

B^+ mode	D mode	Observed Yield	$\epsilon(\%)$	Expected Yield
$D^{*0}\pi^+$	$K^-\pi^+$	166 ± 15	22.3 ± 1.1	$\pm$
	$K^-\pi^+\pi^0$	142 ± 14	10.6 ± 0.6	$\pm$
	$K^0_S\pi^+\pi^-$	24.8 ± 7.5	31.8 ± 0.5	$\pm$
	$K^-\pi^+\pi^+\pi^-$	221 ± 19	18.5 ± 0.8	$\pm$
$D^0\pi^+$	$K^-\pi^+$	286 ± 18	48.2 ± 1.6	$\pm$
	$K^-\pi^+\pi^0$	190 ± 17	10.6 ± 0.7	$\pm$
	$K^0_S\pi^+\pi^-$	43.5 ± 9.2	31.8 ± 1.3	$\pm$
	$K^-\pi^+\pi^+\pi^-$	213 ± 17	18.5 ± 1.0	$\pm$

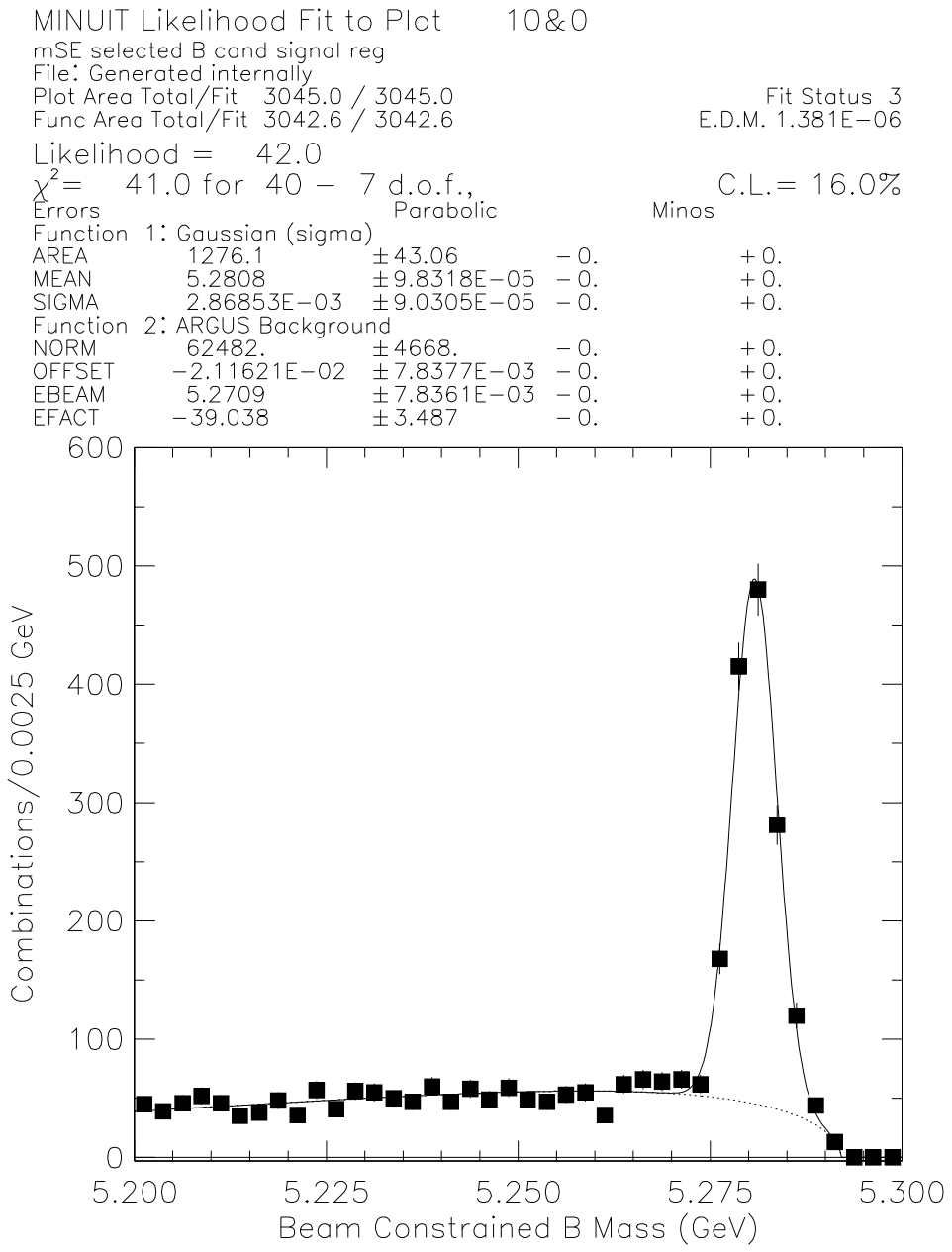

Figure 43: Combined distribution for m_{ES} from all hadronic B^- modes. In some cases, the fit results for individual decay chains suffer from inadequate statistics, particularly without full confidence in Monte Carlo predictions for signal widths.

6 Branching Ratio Measurements

6.1 Final Selections for Branching Ratios

In order to define a candidate acceptance well-within the fiducial volume of *BABAR*, the polar angle range of candidate tracks is restricted to $0.41 < \theta < 2.54$. This also is the region specified by tracking efficiency studies and the methods for optimal B counting [4]. No particle identification requirements are made, in order to eliminate dependence on PID efficiency determination. Finally, we restrict the measurement of absolute branching ratios to the channels $\overline{B}^0 \to D^{*+}\pi^-$ and $\overline{B}^0 \to D^{*+}\rho^-$, where the D^{*+} is reconstructed in the channel $D^0\pi^+$ and the D^0 is seen only in $K^-\pi^+$.

The decay $\overline{B}^0 \to D^{*+}\pi^-$ involves a pseudoscalar initial-state particle decaying into vector and pseudoscalar, so that the final-state D^{*+} is polarized. Therefore, the angle $\theta_H(\pi_S)$ between the soft pion direction and the D^{*+} boost direction in the D^{*+} rest frame, should be distributed as $\cos^2\theta_H(\pi_S)$. In contrast, combinatorial background is uniformly in $\cos\theta_H(\pi_S)$. Therefore, for the $\overline{B}^0 \to D^{*+}\pi^-$ mode, B meson candidates are selected with the additional requirement $\cos\theta_H(\pi_S) > 0.4$. This cut removes 40% of the background and only 5% of signal events.

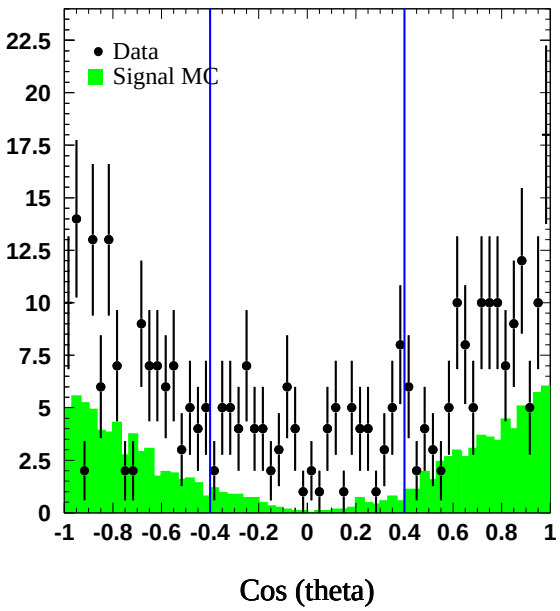

Figure 44: Distribution of the helicity angle of the soft pion, $\cos\theta_H(\pi_S)$, from the decay $\overline{B}^0 \to D^{*+}\pi^-$

6.2 Systematic Studies

6.2.1 *B* Counting

We use the B-counting prescription described in *BABAR* Analysis Document #30 for our B production determination.

We also use the same hadronic event seleciton as is used for B-counting wherever possible. We also automatically require at least 4 tracks per event, since both modes $\overline{B}^0 \to D^{*+}\rho^-$ and $\overline{B}^0 \to D^{*+}\pi^-$ have 4 tracks in the final state. For our tracklists, we use the *GoodTracksLoose* list, which has a requirement on the minimum number of Drift Chamber active hits on track.

If we had exactly the same hadronic event selection, we could use the measurement of the total number of $B\overline{B}$ events which pass the selection for our B counting, which has a systematic error of 1.1%. Our hadronic event selection is not exactly the same as the selection used by the B-counting group, because our Prompt Reconstruction tagbit definition uses the *GoodTracksLoose* and not *ChargedTracks* list. We therefore use the total number of produced $B\overline{B}$ events measurement, which has a systematic error of 1.7% [4].

6.2.2 Tracking Reconstruction Efficiency

We model the *BABAR* detector with a Monte Carlo simulation in order to determine the reconstruciton efficiencies.

The accuracy of our detector simulation for tracking is verified in several ways. Our high momentum charged particle track reconstruction efficiency is measured using a track embedding technique. We select radiative Bhabha events using only Electromagnetic Calorimeter information to avoid any bias from tracking in the selection. The low-multiplicity high-momentum absolute efficiency is determined by measuring the fraction of Bhabha tracks selected by the Calorimeter which are reconstructed as tracks [7].

We then embed these Bhabha tracks into hadronic events and measure both how often the radiative $e^{\pm}$ tracks are reconstructed and how often the hadronic tracks which had been found in the event before we embed the Bhabha tracks are not found after we embed.

Low-momentum charged particle tracking efficiency is measured using a technique which exploits the D^* decay angle distribution [6]. We parameterize the helicity angle distribution as a product of two factors. The first factor describes the efficiency for reconstructing the slow pion from the D^* decay as a function of the pion momentum. The second factor describes the theoretical expectation for the distribution. We then simultaneously fit the helicity distributions from an inclusive sample of D^* events for both the efficiency and the parameters of the helicity distribution. This method allows us to extract the relative detection efficiency for low-momentum charged tracks as a function of their p_T in the lab.

6.2.3 π^0 Reconstruction Efficiency

The π^0 reconstruction efficiency as modeled in our Monte Carlo simulation is verified to be accurate to within 5%.

6.2.4 Cut Variation Systematics

Each of the cuts made in our B candidate selection is individually varied within a reasonable range, in order to determine where there are systematic effects due to uncertainties in our modeling of the acceptance. The distribution of m_{ES} with the varied selection requirement is fit with the ARGUS function to account for the background and a single Gaussian distribution for the B signal. The yield is acceptance corrected to produce a value for the branching ratio with the modified selection criteria. Table 22 summarizes the observed variation of the extracted branching ratio, for each of the selection cuts.

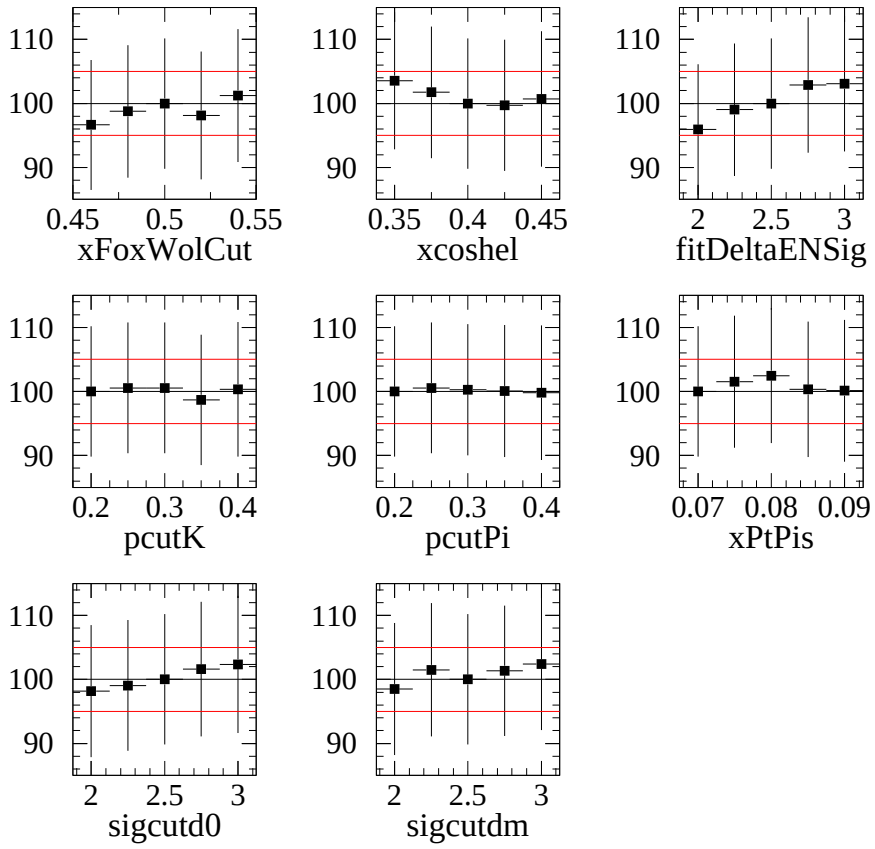

Figure 45: For each variable we use for our B candidate selection, we vary the selection criteria and plot the relative change in the branching ratio, normalized to our default selection. The vertical scale on all plots is the ratio, in percent, of extracted branching ratio normalized to the result for the default selection criteria. The horizontal scale is in units appropriate for each selection criteria. The errors between points are highly correlated. The red lines are at $\pm 5\%$ branching ratio change.

Table 22: For each selection criteria, we measure the effect of a reasonable variation of the requirement on our branching ratio measurement. The efficiencies for this study was estimated using a signal sample produced using the 8 .6.4b SP3 Monte Carlo sample. This Monte Carlo version includes recent improvements in the Drift Chamber efficiency model. No momentum smearing or track killing was used.

Selection Criteria	Value	Variation	Efficiency Change (%)	Branching Ratio Change (%)
D^0 mass	$\pm 2.5\sigma$	$\pm 2.0\sigma$	-1.59	-1.43
		$\pm 3.0\sigma$	-0.57	$+5.29$
Δm	$\pm 2.5\sigma$	$\pm 2.0\sigma$	-4.49	-0.66
		$\pm 3.0\sigma$	$+2.33$	$+0.09$
$\lvert\cos\theta_{D^*}\rvert$	> 0.4	> 0.35	1.62	$+4.31$
		> 0.45	-5.46	$+4.01$
$p(K)$	> 200 MeV	> 300 MeV	0.023	-0.022
$p(\pi_{D^0})$	> 200 MeV	> 300 MeV	-1.11	-0.44
$p(\pi_{\rm soft})$	> 70 MeV	> 80 MeV	-5.02	$+4.86$
		> 90 MeV	-10.46	$+0.41$
π^0 mass	> 120 MeV	> 100 MeV	XX	
		> 130 MeV	XX	
	< 150 MeV	< 170 MeV	XX	
		< 140 MeV	XX	
$E(\gamma)$	> 30 MeV	> 50 MeV	XX	
		> 70 MeV	XX	
lat(γ)	< 0.8	< 2.0	XX	
		< 0.5	XX	
$p(\pi^+_\rho)$	> 100 MeV	> 200 MeV	XX	
		> 300 MeV	XX	
$p(\pi^0_\rho)$	> 100 MeV	> 200 MeV	XX	
		> 300 MeV	XX	
ρ^+ mass	± 150 MeV	± 100 MeV	XX	
		± 200 MeV	XX	
R_2	< 0.5	< 0.49	0.53	-1.20
		< 0.47	-4.83	1.84
$\lvert\cos\theta_{\rm th}\rvert$	< 0.9	< 0.8	XX	
		< 1.0	XX	
ΔE	$< \pm 2.5\sigma$	$< \pm 3.0\sigma$	0.623	$+3.14$
		$< \pm 2.25\sigma$	-3.31	$+4.38$

6.2.5 Particle Identification

We investigated the possibility of using kaon identification to reject backgrounds in the D^0 decay. Varying from no kaon identification to tight kaon identification did not significantly change our signal to background ratio in the $\overline{B}^0 \to D^{*+}\pi^-$ mode. We do see a benefit when

using the SMS "Not A Pion" selector to reject pion backgrounds in the $\overline{B}^0 \to D^{*+}\rho^-$ mode and use it in our selection for the Elba data analysis; however, we will not use it in our final selection.

6.2.6 Branching Ratio Assumptions

The PDG compilation of measured branching ratios for the $D^{*+} \to D^0\pi^+$ and $D^0 \to K^-\pi^+$ are listed in table 23.

Decay Channel	Branching Ratio (%)	Systematic Error (%)
$\Gamma(D^{*+} \to D^0\pi^+)$	68.3 ± 1.4	2.0
$\Gamma(D^0 \to K^-\pi^+)$	3.83 ± 0.09	2.3

Table 23: Branching ratio assumptions for charm decays.

The measurement errors on these branching rations is quoted as a separate systematic error on our final result. We also assume the $\Upsilon(4S)$ decays into $B^0\overline{B}^0$ pairs with a 50% fraction; no systematic error is assigned to this value.

6.3 Branching Ratios

We have measured the branching ratios for the decays $\overline{B}^0 \to D^{*+}\pi^-$ and $\overline{B}^0 \to D^{*+}\rho^-$.

6.4 Additional Checks

In the final version of this analysis, we will produce the helicity distribution for the signal alone, and use the difference between the efficiency corrected number of B decays in the forward and backward directions as a confirmation of our understanding of tracking efficiency.

7 Conclusions

conclusions

References

[1] "Review of Particle Properties", European Physical Journal C3, Number 1–4 (1998).

[2] Charmonium AWG and Tracking Group, "Studies on $K^0_S \to \pi^+\pi^-$ Reconstruction: Status Report", BaBar Analysis Document 019, Version 1 (2000).

[3] Neutral Identification and Reconstruction AWG, "Studies on π^0 Reconstruction: Status Report", BaBar Analysis Document 020, Version 1 (2000).

[4] C.Hearty, "Hadronic Event Selection and B-Counting for Inclusive Charmonium Measurements", *BABAR* Analysis Document 30 (2000).

[5] W.T.Ford, "Choice of Kinematic Variables in B Meson Reconstruction—Take 3", *BABAR* Analysis Document 53 (2000); ΔE is a Lorentz invariant, and could be calculated using lab frame 4-vectors.

[6] O.Long, "Measurement of the slow pion relative efficiency using helicity distributions", *BABAR* Analysis Document 54 (2000).

[7] G.Raven, "Determination of the tracking efficiency for high momentum tracks", *BABAR* Analysis Document 61 (2000).

[8] J.Smith, A.Soffer, and R.Waldi, "Recommendation for Exclsuive B Reconstruction Analysis Variables", *BABAR* Note 497 (1999).

[9] Philip Hart, "Elements of Selecting Good Runs", `http://www.slac.stanford.edu/~philiph/rqm/7mar.pdf` (2000).

[10] `http://www.slac.stanford.edu/BFROOT/www/doc/workbook/nanomicro/v8.6/Micro/Cand_Lists.html`

[11] `http://www.slac.stanford.edu/BFROOT/www/Physics/BaBarData/ChangesSince8.6.2a.html`

[12] M.S. Alam *et al.*, Phys. Rev. **D50** (1994) 43.

[13] E691 Collab., J. C. Anjos *et al.*, Phys. Rev. **D48** (1993) 56.

[14] `http://www.slac.stanford.edu/~chcheng/talk/kpipi0DalitzFunc/index.html`